

Article

Centered Polygonal Lacunary Sequences

Keith Sullivan ¹, Drew Rutherford ² and Darin J. Ulness ^{2,*} ¹ Department of Mathematics, Concordia College, Moorhead, MN 56562, USA; ksulliv1@cord.edu² Department of Chemistry, Concordia College, Moorhead, MN 56562, USA; rutherf@cord.edu

* Correspondence: ulnessd@cord.edu

Received: 16 September 2019; Accepted: 10 October 2019; Published: 11 October 2019



Abstract: Lacunary functions based on centered polygonal numbers have interesting features which are distinct from general lacunary functions. These features include rotational symmetry of the modulus of the functions and a notion of polished level sets. The behavior and characteristics of the natural boundary for centered polygonal lacunary sequences are discussed. These systems are complicated but, nonetheless, well organized because of their inherent rotational symmetry. This is particularly apparent at the so-called symmetry angles at which the values of the sequence at the natural boundary follow a relatively simple $4p$ -cycle. This work examines special limit sequences at the natural boundary of centered polygonal lacunary sequences. These sequences arise by considering the sequence of values along integer fractions of the symmetry angle for centered polygonal lacunary functions. These sequences are referred to here as p -sequences. Several properties of the p -sequences are explored to give insight in the centered polygonal lacunary functions. Fibered spaces can organize these cycles into equivalence classes. This then provides a natural way to approach the infinite sum of the actual lacunary function. It is also seen that the inherent organization of the centered polygonal lacunary sequences gives rise to fractal-like self-similarity scaling features. These features scale in simple ways.

Keywords: lacunary function; gap function; centered polygonal numbers; triangular numbers

1. Introduction

Analytic functions play a predominant role in physics. The isolated singularities of what are otherwise analytic functions often carry much information about the function itself and thereby provide physical insight. Attendant with analytic functions is the power series representation (Taylor or Laurent), whose radius of convergence is restricted by the isolated singularities. Analytically continuing functions outside the radius of convergence was the focus of much of the early work on analytic functions was on developing methods to [1,2].

There are occasions, however, when the singularities condense into a curve through which analytic continuation is not possible. The curve in the complex plane mapped out by this set of singularities is called a natural boundary. A particularly important class of functions that exhibit a natural boundary are the lacunary functions, also called gap functions [1,3]. Lacunary functions are characterized by a Taylor series that has “gaps” (or “lacunae”) in the progression of powers. That is, only certain powers in the power series are active. A prototype example is $f(z) = \sum_{n=1}^{\infty} z^{n^2} = z + z^4 + z^9 + z^{16} + \dots$. Associated with $f(z)$ is a lacunary sequence whose members are of the form $f(z) = \sum_{n=1}^N z^{n^2}$, $N > 0 \in \mathbb{Z}$.

If the gaps in the powers increase such that the gap tends to infinity as $n \rightarrow \infty$, then the function will exhibit a natural boundary. This is true by the celebrated gap theorem of Hadamard [1]. In the example function above, the natural boundary is the entire unit circle. $f(z)$ is analytic in the open unit disk.

It is often stated that most functions are lacunary and only special ones have isolated singularities [1,2]. This statement is at the heart of the connection between lacunary and the so-called random series [1,2]. But of course, those special (meromorphic) functions are precisely what have proven so useful in physics and chemistry; hence there are by far more familiar to physicists and chemists. The undesirable behavior of the lacunary functions have limited their use in application to physical problems. Nevertheless, lacunary functions have been investigated in some physical settings recently.

The presence of natural boundaries has been shown to have real physical consequences. In particular, Creagh and White showed that natural boundaries can be important in the short-wavelength approximation when calculating evanescent waves outside of elliptic dielectrics [4]. Meanwhile, Greene and Percival discussed natural boundaries in the context of Hamiltonian maps in the area of integrable/nonintegrable systems [5]. Also, Shado and Ikeda have demonstrated that natural boundaries impact quantum tunneling in some systems by influencing instanton orbiting [6].

In the statistical mechanics of Ising-like models, Guttman et al. have shown that if the system is not solvable then any solution must be expressible in terms of functions having natural boundaries [7,8]. Indeed, Nickel has explicitly shown the presence of a natural boundary in the calculation of the magnetic susceptibility in the 2D Ising model [9]. Quite recently, Yamada and Ikeda have investigated wavefunctions associated with Anderson-localized states in the Harper model in quantum mechanics [10]. In kinetic theory, lacunary functions exhibit features upon approaching the natural boundary that are related to Weiner (stochastic) processes. As such, lacunary functions have been discussed in the context of Brownian motion [1,11].

In addition to physics, lacunary functions are useful in probability theory. There are lacunary trigonometric systems which behave like independent random variables. Indeed, they are governed by the central limit theorem [2,12–14]. The study of harmonic analysis on compact groups have benefited from the study of Lacunary trigonometric systems [15,16]. The same is true in the area of incomplete Gaussian summations [17–20], and the Jacobi theta functions [21–24].

The goal of this current work is to provide general insight into lacunary functions, but, more particularly, to discuss features of what are referred to in this work as *centered polygonal lacunary functions*. This is the family of lacunary functions where the active terms in the Taylor series are those in which the powers are centered polygonal numbers (cpns) [25]. These lacunary functions, as well as their associated finite sequences, exhibit several unique properties. Unlike general lacunary functions, they have true rotational symmetry and their level sets are polished. These concepts will be discussed in the subsequent sections.

The behavior and characteristics of the natural boundary for centered polygonal lacunary sequences are extremely complicated. Nonetheless, they are well organized because of the inherent rotational symmetry of the centered polygonal lacunary functions. This is particularly apparent at the so-called symmetry angles, where the value at the natural boundary follows a relatively simple $4p$ -cycle. The introduction of fibered spaces can organize these cycles into equivalence classes. This then provides a natural way to approach $N = \infty$. The inherent organization of the centered polygonal lacunary sequences gives rise to fractal-like self-similarity scaling features. Indeed, the current authors have recently investigated fractal and scaling behavior of centered polygonal lacunary functions [26,27]. It is hoped that the current work will add to the foundational understanding of that earlier work.

After laying down some notation and definitions as well as several different ways of visualizing these functions, this work focuses on several special aspects of centered polygonal lacunary functions and their associated sequences. First, the limit values of the members of the centered polygonal lacunary sequences at the natural boundary form their own sequence. This sequence has interesting and well-organized cycles. This is brought into the foreground through the use of a fibered space representation which leads to a reduction of the infinite sequence to a finite sequence of equivalence classes.

At the natural boundary itself, the centered polygonal lacunary functions reduce to centered polygonal lacunary trigonometric systems. These systems have interesting scaling properties and fractal-like characteristics.

Next, the symmetry angles (defined below) form special radial paths from the origin to the natural boundary. A few of the properties of the centered polygonal lacunary functions along these paths are explored. In doing so, a particularly simple asymptotic dependence of the maximum of these functions on the particular symmetry angle is discovered.

This work then proceeds in investigating the structure of the limiting values at the natural boundary of centered polygonal lacunary sequences along symmetry angles. These special infinite sequences will be referred to here as *p*-sequences. They arise by taking the limit of the centered polygonal lacunary sequence on the unit circle and at integer fractions of the rotational symmetry angle. One focus of this work will be the exploration of some of the structural features of the *p*-sequences. Notably, the relationship between the cpns and the well-known triangle numbers along with properties of the lacunary sequences at the natural boundary allows one to discuss many features in a way that is independent of the type of cpn used. That is, the entire family of centered polygonal lacunary sequences have the same structural features.

In the current work, all of the numerical calculations were direct summation of the lacunary sequence members. This was carried out with MATHEMATICA. Yamada and Ikeda have recently investigated the use of Padé approximate methods for speeding up the convergence of summations for lacunary functions [10,28].

2. Notation and Basic Definitions

We consider a *lacunary sequence* of functions, with the *N*th member of the sequence given by

$$f_N(z) = \sum_{n=1}^N z^{g(n)}, \tag{1}$$

where $g(n)$ is a function of n satisfying the conditions of Hadamard’s gap theorem [1]. Note that the sum starts at $n = 1$. It certainly could be defined to start at $n = 0$ but there are some desirable reasons to use the former as the definition. In Section 5, the relation to series beginning at $n = 0$ is discussed. For $g(n) = n$ we recover

$$f_N(z) = \sum_{n=1}^N z^n \xrightarrow{N=\infty} \frac{z}{1-z}, \tag{2}$$

which is closely related to the geometric series and is not lacunary.

For notational convenience we define

$$\mathfrak{L}(g; z) \equiv \left\{ f_N(z) = \sum_{n=1}^N z^{g(n)} \right\}, \tag{3}$$

to represent the particular lacunary sequence described by $g(n)$, in complex variable z . The condensed notation $f_N(z)$ will be used throughout to represent the *N*th member of $\mathfrak{L}(g; z)$. Some examples which illustrate the notation are:

- $\mathfrak{L}(n^2; z) \equiv \left\{ f_N(z) = \sum_{n=1}^N z^{n^2} \right\}$
- $\mathfrak{L}(n!; z) \equiv \left\{ f_N(z) = \sum_{n=1}^N z^{n!} \right\}$
- $\mathfrak{L}(n^2; \rho e^{i\pi/3}) \equiv \left\{ f_N(z) = \sum_{n=1}^N (\rho e^{i\pi/3})^{n^2} \right\}$.

It is worth highlighting that there are *N* terms in the summations and that the sum truncates after the $g(N)$ th power.

2.1. Centered Polygonal Numbers

Centered polygonal numbers (cpns) are an infinite, increasing sequence of numbers associated with points on a polygonal lattice [25]. These numbers were discussed in the context of two-dimensional crystal structures by Teo and Sloane [29]. The formula for the centered k -gonal numbers is

$$C^{(k)} = \left\{ \frac{kn^2 - kn + 2}{2} \right\}, \quad n \geq 1. \tag{4}$$

When it is necessary to identify a particular member of $C^{(k)}$, the notation $C^{(k)}(j)$ will be used for the j th member of the set.

The cpns have a special feature when considering differences between numbers within a set that is deeply related to the unique behavior of their corresponding lacunary functions. Consider the set of numbers $C^{(k)}$ and, further, consider the set generated by taking all possible non-zero, positive differences between these numbers: $\Delta C^{(k)} \equiv \{C^{(k)}(p) - C^{(k)}(q)\}, p > q$ (There is, of course, a similar set where all differences are negative). The following observations are made without proofs given here.

- All members of $\Delta C^{(k)}$ are divisible by k .
- The difference between the $(m + n)$ th and the n th term is

$$C^{(k)}(m + n) - C^{(k)}(n) = k \left(mn + \frac{m(m - 1)}{2} \right) \tag{5}$$

- The “normalized” set $\Delta C = \Delta C^{(k)} / k$ is independent of k .
- All integers are represented in $\Delta C^{(k)} / k$ although, for any truncated set $C^{(k)}$ having a finite P number of members, there are missing integers. The first of which is 2^m , where m is the value such that $2^m > P$.
- Some integers are represented more than once.

The centered polygonal numbers are related to the polygonal numbers, where the n th term of a k -gon is

$$P^{(k)}(n) = \frac{n^2(k - 2) - n(k - 4)}{2}, \quad n \geq 1. \tag{6}$$

Lemma 1. $P^{(k)}(n) + (n - 1)^2 = C^{(k)}(n)$.

Proof.

$$\begin{aligned} P^{(k)}(n) + (n - 1)^2 &= \frac{n^2(k - 2) - n(k - 4)}{2} + n^2 - 2n + 1 \\ &= \frac{n^2(k - 2) + 2n^2 - n(k - 4) - 4n + 2}{2} \\ &= \frac{kn^2 - kn + 2}{2} = C^{(k)}(n). \end{aligned} \tag{7}$$

□

Of particular importance in this work is the special case of triangular numbers,

$$T \equiv P^{(3)} = \left\{ \frac{n^2 + n}{2} \right\} = \left\{ \frac{n(n + 1)}{2} \right\}. \tag{8}$$

(Note: T is the formula for the sum of the integers 0 through n). Again, $T(j)$ will represent the j th member of T . The following lemma is immediate.

Lemma 2.

$$\frac{C^{(k)}(m+1) - 1}{k} = T(m). \tag{9}$$

Proof.

$$\begin{aligned} \frac{1}{k} \left(\frac{k(m+1)^2 - k(m+1) + 2}{2} - 1 \right) &= \frac{1}{k} \left(\frac{km^2 + 2km + k - km - k + 2 - 2}{2} \right) \\ &= \frac{1}{k} \left(\frac{km^2 + km}{2} \right) = T(m). \end{aligned} \tag{10}$$

□

This simple connection of (all) cpns to the triangular numbers will prove to be very valuable for two reasons. First, many of the theorems can be reduced to the corresponding theorem for triangular numbers. Second, any features of the centered polygonal lacunary functions that are inherently connected to the triangle numbers are independent of k . It turns out that these are the features that distinguish the family of centered polygonal lacunary functions from more general lacunary functions.

The following lemma contains results that will be used in later sections. The proof is straightforward; hence it is not given.

Lemma 3. $C^{(k)}(i)$ be the i th centered k -gonal number. Expressions for $C^{(k)}(i) + C^{(k)}(j)$ are in the upper half triangle (including the diagonal) of the table below. Expressions for $C^{(k)}(i) - C^{(k)}(j)$ are given in the lower triangle of the table below.

	$C^{(k)}(1)$	$C^{(k)}(2)$	$C^{(k)}(3)$	$C^{(k)}(4)$
$C^{(k)}(1)$	2	$k + 2$	$3k + 2$	$6k + 2$
$C^{(k)}(2)$	k	$2k + 2$	$4k + 2$	$7k + 2$
$C^{(k)}(3)$	$3k$	$2k$	$6k + 2$	$9k + 2$
$C^{(k)}(4)$	$6k$	$5k$	$3k$	$12k + 2$

2.2. Features of Lacunary Sequences

It proves most revealing, for this work, to consider members of $\mathfrak{L}(g; z)$ in their polar form: $f_N(z) = R(z)e^{i\Phi(z)}$ and to focus on $R(z) = |f_N(z)|$, although $f_N(z)$ itself will also be discussed. Figure 1 illustrates how the functions will best be visualized for this work. The example of $\mathfrak{L}(C^{(3)}; z)$ is used. The top row shows a surface and contour plot of $|f_{32}(z)|$. The unity level set, $|f_N(z)| = 1$ will be the center of much of the discussion in subsequent sections. The plot on bottom left of Figure 1 shows a contour plot limited from $|f_N(z)| = 0$ to $|f_N(z)| = 1$. The plot on the bottom right shows what is termed the *main unity contour*.

Definition 1. Main unity contour. The simple closed rectifiable curve marking the boundary of the set of points, z , such that $|f(z)| \leq 1$ and are path-connected to the origin.

Note that the main unity contour is distinct from the full unity contour (unity level set). The (infinite number of) curves bounding sets not path-connected to the origin are not part of the main unity contour while they are part of the unity level set.

The main unity contour is immensely complicated in that it is an infinite order implicit function of radius, ρ , and polar angle, ϕ . It represents the set of values of ρ and ϕ for which the terms in the infinite sum representation of the lacunary function conspire to yield $R(z) = 1$. Figure 2 shows the same graphical representation as the bottom left plot in Figure 1 for the cases of $\mathfrak{L}(C^{(k)}; z)$, where $k = 1, \dots, 12$.

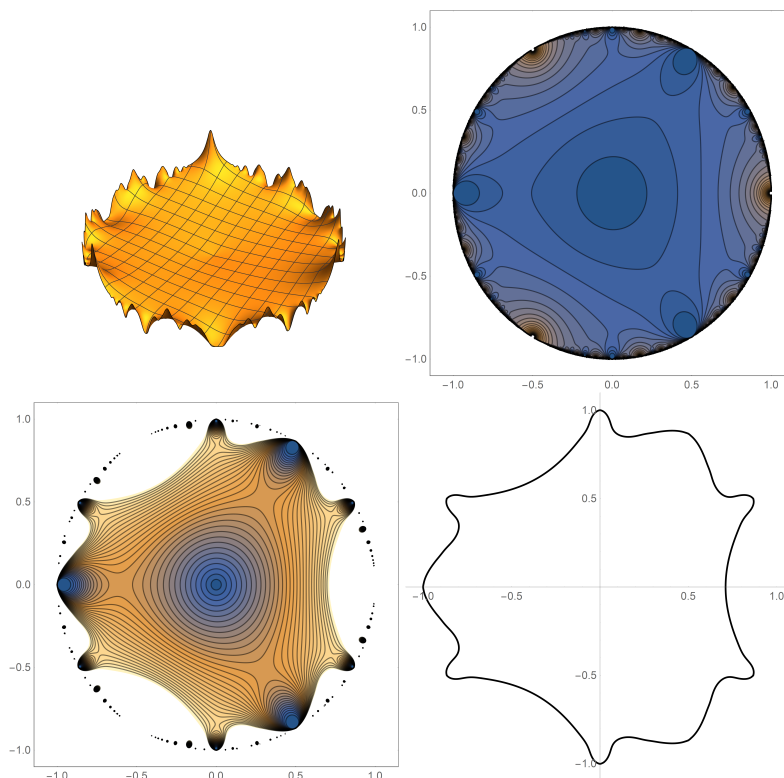


Figure 1. Important ways to present graphs illustrated by the example of $\mathfrak{L}(C^{(3)}; z)$. The top row is a surface and contour plot of $|f_{32}(z)|$. The surface is plotted out to $\rho = 0.95$ in order to give a good view of the surface structure as it approached the natural boundary. For larger values of ρ the singularities of the natural boundary dominate the graph and obstruct the view. The bottom row representations are particularly useful for this work. The contour plot is truncated at the unity level set and shown on the left and only the main contour of the unity level set is shown on the right. For the contour plots, blue shading represents low values and orange shading represents high values.

A heuristic viewing of Figures 1 and 2 reveals several important concepts which will be fleshed-out in the sections below. Additionally, it is helpful to view a sampling of lacunary functions that are not built from the cpns. Twelve such functions are collected in Figure 3. These include the $g(n) = n^m, m^n$ families, as well as, $g(n) = n!, \text{fib}(n)$, where $\text{fib}(n)$ are the Fibonacci numbers. Finally, $g(n) = n \ln n$ shows an example of a case where a branch cut is present.

Two important distinctions emerge when comparing Figure 2 with Figure 3. First, the cpn-based functions have k -fold rotational symmetry. For the non-cpn-based functions the perfect k -fold symmetry is lost. However, a k -fold rotational quasi-symmetry is very apparent. Second, the unity level set appears much smoother for the cpn-based lacunary functions than for the non-cpn-based ones. The word smooth must be avoided as a visual descriptor because it is not to be implied that the unity level set curve will be smooth in the sense of having all its derivatives at every point. This is true for finite N but not necessarily for $N = \infty$. The word “polished” will be used in place of smooth. Inspection of the unity level set curves in Figure 3 shows that these curves are not polished and therefore are “rough.” Rotational quasi-symmetry and polishness are discussed in subsequent sections.

A few more comments are in order. Mirror symmetry about the real line and the emergence of the natural boundary structure on the unit circle are common features between cpn-based and non-cpn-based lacunary functions. The mirror symmetry between the upper and lower half-planes is a result of the general properties of the modulus of a function. Parts of the natural boundary appear because it is not simply a wall of singularity at the unit circle, but rather it is a dense curve of both singularities and zeros. The plots in Figures 2 and 3 pick up some of the emerging zeros. Taking the sums out to larger N values causes more of these features to appear along the unit circle.

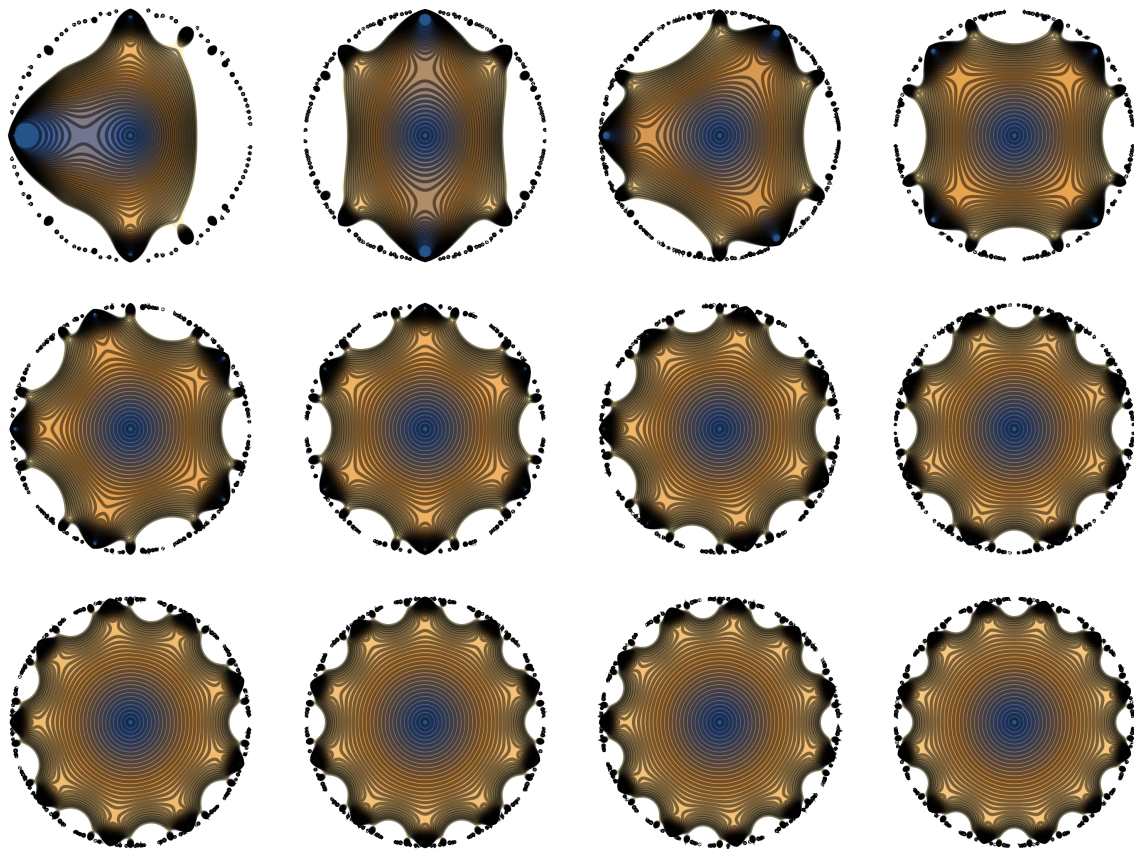


Figure 2. Contour plot of $|\mathfrak{L}(C^{(k)}; z)|$ for $k = 1$ to $k = 12$ and $N = 16$. The 30 contours (level sets) in each graph are plotted from 0 to 1. Blue shading represent low values and orange shading represents high values. The rotational symmetry (equal to k) of the graphs are visually apparent. Further, the contours are not rough (referred to here as “polished”). Both of these features are special to centered polygonal lacunary sequences.

A few concrete definitions can be put into place.

Definition 2. *Primary symmetry.* The rotational symmetry of the $N = 2$ member of $|\mathfrak{L}(g; z)|, |f_2(z)|$, is called the primary symmetry.

Theorem 1. The primary symmetry of $|\mathfrak{L}(g(n); z)|$ is $k = g(2) - g(1)$.

Proof. Casting z as $\rho e^{i\phi}$ results in

$$\begin{aligned}
 |f_2(z)| &= \sqrt{\left((\rho e^{-i\phi})^{g(1)} + (\rho e^{-i\phi})^{g(2)} \right) \left((\rho e^{i\phi})^{g(1)} + (\rho e^{i\phi})^{g(2)} \right)} \\
 &= \sqrt{\rho^{2g(1)} + \rho^{2g(2)} + \rho^{g(2)+g(1)} (e^{i(g(2)-g(1))\phi} + e^{-i(g(2)-g(1))\phi})} \\
 &= \sqrt{\rho^{2g(1)} + \rho^{2g(2)} + 2\rho^{g(2)+g(1)} \cos((g(2) - g(1))\phi)}.
 \end{aligned}
 \tag{11}$$

This implies $|f_2(z)|$ has primary symmetry of $k = g(2) - g(1)$, completing the proof. \square

Corollary 1. The primary symmetry of the centered polygonal lacunary functions is k .

Proof. Consider

$$\frac{4k - 2k + 2}{2} - \frac{k - k + 2}{2} = k. \tag{12}$$

□

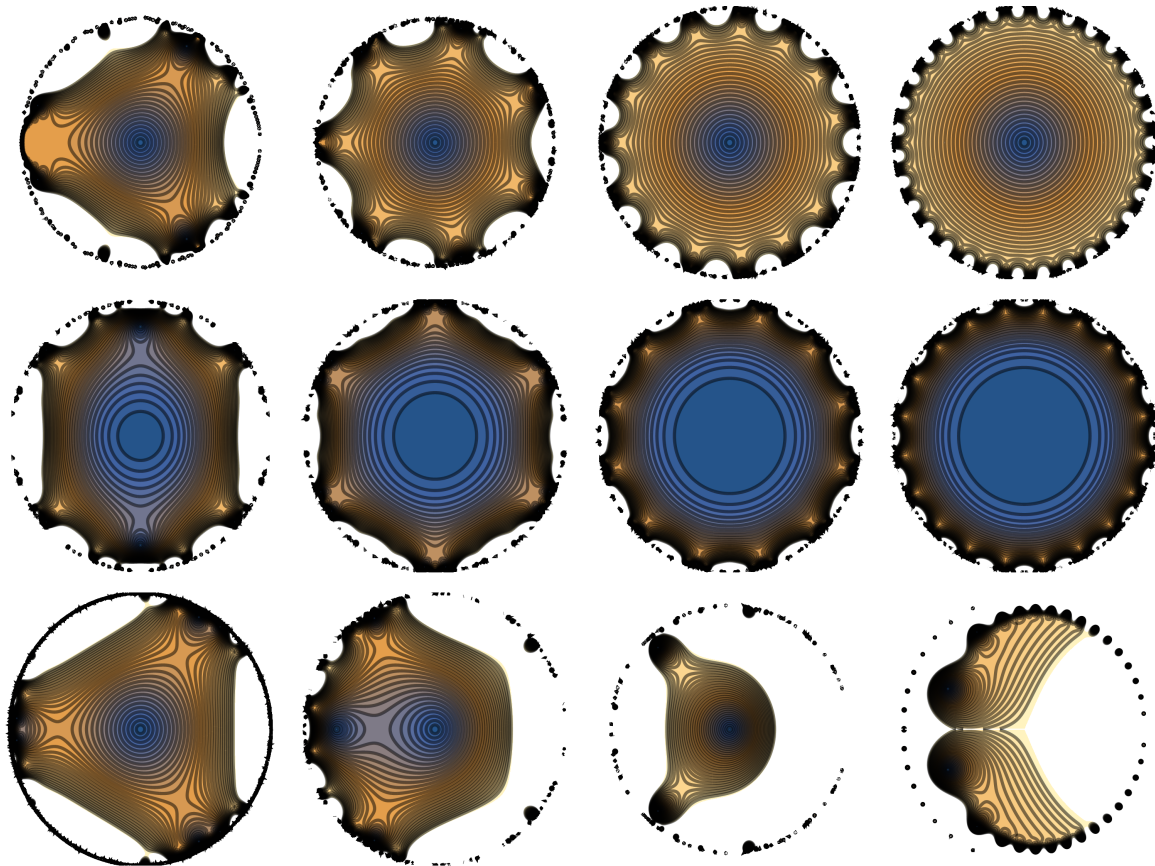


Figure 3. Contour plot of $|\mathcal{L}(g(n); z)|$ for a variety of $g(n)$ and $N = 16$. The 30 contours (level sets) are plotted from 0 to 1. Blue shading represent low values and orange shading represents high values. The top row is $g(n) = n^m$ for $m = 2, 3, 4, 5$. The second row is $g(n) = m^n$ for $m = 2, 3, 4, 5$. The third row is $g(n) = n^n$, $g(n) = n!$, $g(n) = \text{fib}(n)$, where $\text{fib}(n)$ is the n th Fibonacci number and $g(n) = n \ln n$. The strict rotational symmetry is broken but a quasi-rotational symmetry persists for all but the last three cases. In contrast to the plots of Figure 2, the contours are rough in all cases. This is typically the case for general lacunary functions.

Definition 3. *Symmetry angle.* Let the primary symmetry be k -fold. The first symmetry angle is $\alpha_1 = \frac{\pi}{k}$, $k \in \mathbb{Z}^+$. The p th symmetry angle is $\alpha_p = \frac{\pi}{pk}$, $p, k \in \mathbb{Z}^+$.

Definition 4. *p th symmetry zeros.* The zeros of the cpn -based lacunary functions $|f_N(z)|$ are the zeros encountered along the radial segment from the origin to the natural boundary for segments at integer multiples of the p th symmetry angle.

The lacunary sequence $|\mathcal{L}(C^{(3)}; z)|$ can serve as an illustrative example of the above definitions. One calculates the primary symmetry to be $k = 3$. The first symmetry angle is $\frac{\pi}{3}$, the second is $\frac{\pi}{6}$, third is $\frac{\pi}{9}$, etc. The first symmetry zeros are most pronounced but the second symmetry zeros are also very evident (see Figure 1). In this particular case, the first and second symmetry zeros lie inside the main unity level set, where as higher symmetry zeros are exterior to it.

3. Spherical Mappings

As a complement to the visualization of the centered polygonal lacunary functions just discussed, two distinct mapping schemes of the complex plane to the surface of the unit sphere are presented in this section. The first is simply the inverse stereographic projection and the second maps the unit disk to the entire sphere such that its boundary maps to the single point at the south pole.

3.1. Hemisphere Mapping: Inverse Stereographic Projection

The inverse stereographic projection maps the full complex plane onto the sphere. The interior of the unit disk is mapped to the northern hemisphere, while the exterior of the unit sphere is mapped to the southern hemisphere. If the point at infinity is included, it is mapped to the south pole. For this mapping, it is nice to consider the natural piece-wise function made from $\mathfrak{L}(C^{(k)}; z)$ and $\mathfrak{L}(C^{(k)}; 1/z)$,

$$|F_N(z)| = \begin{cases} f_N(z) & |z| \leq 1 \\ f_N\left(\frac{1}{z}\right) & |z| > 1, \end{cases} \tag{13}$$

rather than simply $f_N(z)$. This produces a mirror image of the northern hemisphere on the southern hemisphere. The natural boundary is at the equator. The example for $k = 4$ is shown in Figure 4.

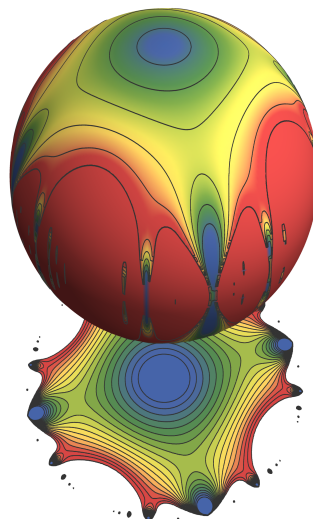


Figure 4. Inverse stereographic projection of the piecewise function $\mathfrak{L}(C^{(4)}; z)$ for $z < 1$ and $\mathfrak{L}(C^{(4)}; 1/z)$ for $z > 1$. Here, the natural boundary gets mapped to the equator. The northern hemisphere is the image of the interior of the unit disk, while the southern hemisphere is the image of the exterior of the unit disk.

3.2. Whole Sphere Mapping: Condensing the Natural Boundary

Let the coordinates of the surface of the unit sphere be ϑ (polar angle) and φ (azimuth angle). Then, the transformation

$$\begin{aligned} x &= \cos \varphi \sin \frac{\vartheta}{2} \\ y &= \sin \varphi \sin \frac{\vartheta}{2}, \end{aligned} \tag{14}$$

provides a mapping from the unit disk to the unit sphere, where $z = 0$ maps to the north pole and $|z| = 1$ maps to the south pole. This mapping offers a potential advantage of mapping the entire natural boundary to a single point, which could help handle its singular nature in some applications. Notably, $\int_0^{2\pi} f_N(e^{i\varphi}) = 0$ for finite N . Perhaps in some physical settings this might reasonably be

extended to $N = \infty$. As such, the value of f_N at the south pole could be assigned zero. Even in cases where this might be reasonable, there still remains singular behavior on the approach to the south pole.

Figure 5 shows provides an illustrative example for the case of $\mathfrak{L}(C^{(4)}; z)$. The rotational symmetry remains clearly exposed, particularly from the “bottom” (looking up at the south pole) shown in the bottom left panel of Figure 5. This view also nicely shows the condensation of the natural boundary into a point.

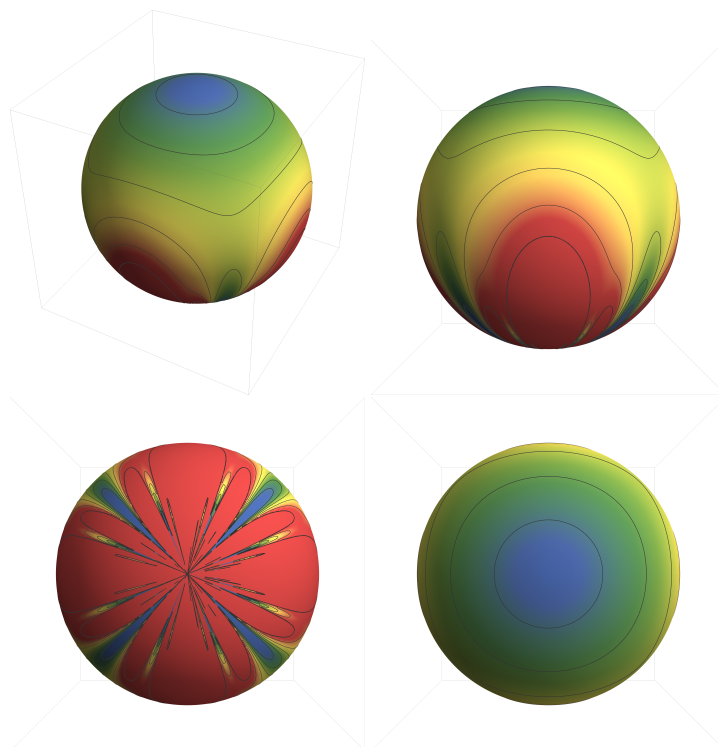


Figure 5. Various viewpoints of the whole sphere mapping of $\mathfrak{L}(C^{(4)}; z)$ for the case of $|f_{12}(z)|$. The natural boundary is mapped to the south pole and is seen most clearly in the bottom left panel.

4. Symmetry

Turning attention to the rotational and quasi-rotational symmetry of the main unity contour of $|f_N(z)|$, we consider the lacunary sequence along the positive real axis, $\mathfrak{L}(C^{(k)}; \rho)$, compared to that along the first symmetry angle, $\mathfrak{L}(C^{(k)}; \rho e^{i\frac{\pi}{k}})$. Along the real line, $|f_N(z)| = f_N(\rho)$, so expanding the series to the first few terms, simplifying, and using Lemma 2 leads to

$$|f_N(\rho)| = \left(\rho + \rho^{k+1} + \rho^{3k+1} + \rho^{6k+1} + \rho^{10k+1} + \dots \right) = \sum_{n=1}^N \rho^{1+kT(n)}. \tag{15}$$

Along the first symmetry angle $|f_N(z)| = f_N(\rho \cos(\pi/k))$, so

$$f_N \left(\rho \cos \frac{\pi}{k} \right) = \sum_{n=1}^N \rho^{1+kT(n)} \left(\cos \frac{\pi}{k} \right)^{1+kT(n)}. \tag{16}$$

One now compares the ratio of second term along the positive real axis and along the first symmetry angle with the ratio of the third term along the positive real axis and along the first symmetry angle. The ratios are

$$\frac{\text{2nd term, real axis}}{\text{2nd term, first symmetry axis}} = \frac{1}{\left(\cos \frac{\pi}{k} \right)^{k+1}} \tag{17}$$

and

$$\frac{\text{3rd term, real axis}}{\text{3rd term, first symmetry axis}} = \frac{1}{\left(\cos \frac{\pi}{k}\right)^{3k+1}}. \tag{18}$$

This suggests the symmetry determined by the second term (the primary symmetry) is much stronger than that introduced by higher order terms. This is consistent with what is seen visually in Figure 2. By way of example, for $k = 3$ the primary symmetry is 64 times stronger. This reduces to about 2.3 for the case of $k = 12$.

The fact that the comparison of ratios did not employ the rotational symmetry of the full function allows for this to be used with quasi-rotational symmetry as well. Consider the case of $\mathcal{L}(n^2; z)$. This has a primary symmetry of $k = 3$ and one visually sees a 3-fold quasi-rotational symmetry as well (see Figure 3). Carrying out the calculation of the ratios, one finds that the second term is $512/16 = 32$ times stronger than the higher order terms. As a result, the quasi-rotational symmetry for $\mathcal{L}(n^2; z)$ is quite pronounced. As a third example one finds a ratio comparison of 2^{23} in the case of $\mathcal{L}(n^n; z)$, again consistent with what is visually apparent in Figure 3. Lastly, as a null-example, we consider $\mathcal{L}(n!; z)$ from Figure 3. The primary symmetry is determined to be $k = 1$ and the ratio of the third term is the same as the second term. Consequently, no quasi-rotational symmetry beyond 1-fold is present.

The real and imaginary parts of $f_{16}(z)$ for the case of $\mathcal{L}(C^{(3)}; z)$ are shown in Figure 6. In striking contrast to $|f_{16}(z)|$, the real and imaginary parts neither exhibit rotational symmetry nor polishness. However, it is revealing to plot the zero level sets for these parts. These contours are superimposed on $|f_{16}(z)|$ in the bottom right panel of Figure 6.

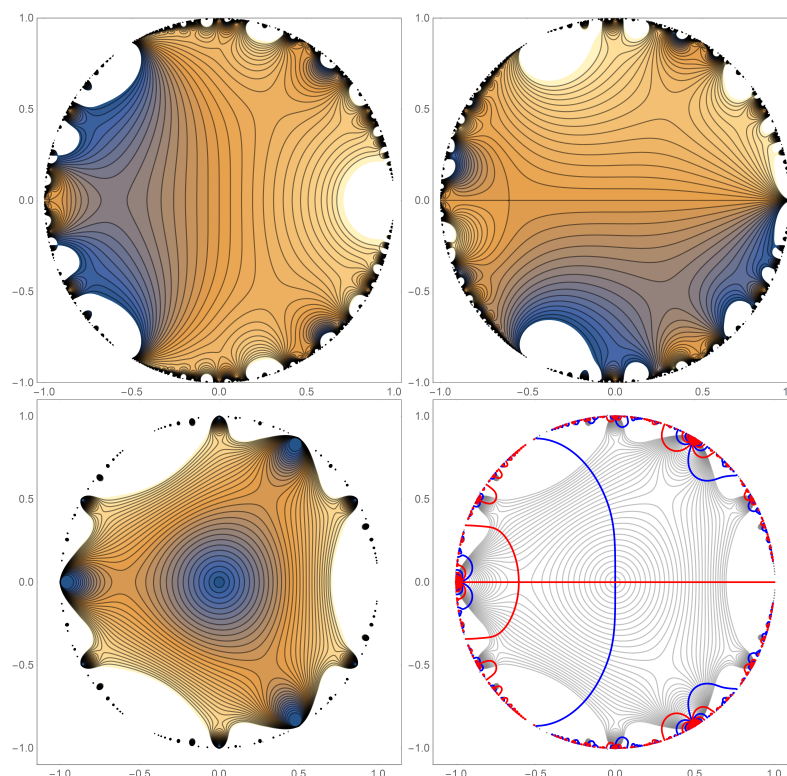


Figure 6. The case of $\mathcal{L}(C^{(3)}; z)$. The top row consists of plots of the real part (left) and imaginary part (right) of $f_{16}(z)$. The bottom left graph is of $|f_{16}(z)|$ exactly as in Figure 2. The bottom right shows $|f_{16}(z)|$ superimposed with the zero curves of the real (blue) and imaginary (red) parts of $f_{16}(z)$. Of note is that the real and imaginary parts do not carry the symmetry nor polishness of the modulus.

Turning attention to another interesting case, it is enjoyable to consider the $k \rightarrow \infty$ limit of $\mathfrak{L}(C^{(k)}; z)$. Thus,

$$\lim_{k \rightarrow \infty} \sum_{n=1}^N z^{C^{(k)}(n)}. \tag{19}$$

Here the primary symmetry is (via Theorem 1 and Lemma 3)

$$\lim_{k \rightarrow \infty} C^{(k)}(2) - C^{(k)}(1) = \lim_{k \rightarrow \infty} k = \infty; \tag{20}$$

the symmetry of a circle. Further, the main unity contour gets pushed out to the natural boundary and $|f(z)| = \rho$ has the shape of a cone in the unit disk.

In this limiting case, the natural boundary has a great deal of regularity but is also very active. The first symmetry zeros become dense around the entirety of the unit circle. This is also the case for the second, third, etc., symmetry zeros and the intervening infinities.

5. Recurrence Relations, Relations to General Lacunary Functions and Other Transformations

In this section a recurrence relation between $C^{(2)}$ and $C^{(k)}$ based lacunary sequences is shown. Also connection to series that start with $n = 0$ is made. Finally, these systems are cast in terms of the Jacobi theta functions.

First, however, the issue of beginning the summation at $n = 0$ is addressed. The formula for $C^{(k)}$ given in Equation (4), but starting at $n = 0$, can be recast as

$$C^{(k)} = \left\{ \frac{kn^2 + kn + 2}{2} \right\}, \quad n \geq 0. \tag{21}$$

This allows one to write the lacunary series starting at $n = 0$;

$$\sum_{n=1}^N z^{\frac{kn^2 - kn + 2}{2}} = \sum_{n=0}^{N-1} z^{\frac{kn^2 + kn + 2}{2}}. \tag{22}$$

5.1. Relationship between Lacunary Sequences

Several relationships between lacunary sequences are now listed as theorems.

Theorem 2.

$$\mathfrak{L}(C^{(k)}; z) = z^{1-k} \mathfrak{L}(C^{(2)}; z^k). \tag{23}$$

Proof. The summation representation of the N th member of $\mathfrak{L}(C^{(k)}; z)$ is manipulated via elementary properties of exponents as

$$\begin{aligned} \sum_{n=1}^N z^{\frac{kn^2 - kn + 2}{2}} &= \sum_{n=1}^N z^{\frac{k}{2}(2n^2 - 2n)} z = \sum_{n=1}^N z^{\frac{k}{2}(2n^2 - 2n)} z^{\frac{2k}{2}} z^{-\frac{2k}{2}} z \\ &= \sum_{n=1}^N z^{\frac{k}{2}(2n^2 - 2n + 2)} z^{1-k} = z^{1-k} \sum_{n=1}^N \left(z^k \right)^{\frac{2n^2 - 2n + 2}{2}}. \end{aligned}$$

The last expression is $z^{1-k} \mathfrak{L}(C^{(2)}; z^k)$ which completes the proof. \square

The critical implication of this theorem is that much of the study of centered polygonal lacunary functions can be reduced to the study of those based on triangular numbers.

Theorem 3.

$$\mathfrak{L}(C^{(k)}; z) = z \sum_{n=0}^{N-1} \left(z^k \right)^{T(n)}. \tag{24}$$

Proof. Starting from the right hand side of the theorem and using Equation (8), one sees

$$z \sum_{n=0}^{N-1} \binom{n^2+n}{z^k}^{\frac{n^2+n}{2}} = \sum_{n=0}^{N-1} z^{\frac{kn^2+kn+2}{2}} = \sum_{n=1}^N z^{\frac{kn^2-kn+2}{2}}. \tag{25}$$

The last expression is $\mathfrak{L}(C^{(k)}; z)$ which completes the proof. \square

Theorem 4.

$$\mathfrak{L}(C^{(k)}; z) = \mathfrak{L}(P^{(k)} + (n - 1)^2; z^k). \tag{26}$$

Proof. The proof follows immediately from Lemma 1. \square

One can consider $\mathfrak{L}(C^{(k)}; z)$ at the natural boundary. Here, $z = \rho_1 e^{i\phi}$, where $\rho_1 = \lim_{\rho \rightarrow 1-}(\rho)$ and 1_- means approaching unity from below. Under these conditions we write

$$f_N(\rho_1 e^{i\phi}) = \sum_{n=1}^N \rho_1^{C^{(k)}(n)} e^{i(C^{(k)}(n))\phi}. \tag{27}$$

Moving to the modulus and temporarily considering the mod-square,

$$\begin{aligned} |f_N(\rho_1 e^{i\phi})|^2 &= \left| \sum_{n=1}^N \rho_1^{C^{(k)}(n)} e^{i(C^{(k)}(n))\phi} \right|^2 \\ &= \sum_{n=1}^N \rho_1^{C^{(k)}(n)} e^{i(C^{(k)}(n))\phi} \sum_{m=1}^N \rho_1^{C^{(k)}(m)} e^{-i(C^{(k)}(m))\phi} \\ &= \sum_{n=1}^N \sum_{m=1}^N \rho_1^{C^{(k)}(n)+C^{(k)}(m)} e^{i(C^{(k)}(n)-C^{(k)}(m))\phi}. \end{aligned} \tag{28}$$

This double summation can be recast as a single summation over “self-terms” and a double summation over “cross-terms.” Doing this yields

$$|f_N(\rho_1 e^{i\phi})|^2 = \sum_{j=1}^N \rho_1^{2C^{(k)}(j)} + \sum_{n=1}^N \sum_{m=1}^N \rho_1^{C^{(k)}(m)+C^{(k)}(n)} e^{i(C^{(k)}(n)-C^{(k)}(m))\phi}. \tag{29}$$

Setting aside the self-term, setting $\rho_1 = 1$, and employing the Euler identity for cosine, the double sum can be recast as the nested double sum

$$|f_N(\rho_1 e^{i\phi})|_{\text{trig}}^2 = 2 \sum_{p=2}^N \sum_{m=1}^p \cos(k\Delta C(pq)\phi), \tag{30}$$

where $\Delta C(pq)$ is the pq th term in the normalized difference set of cpns, ΔC (defined above). This equation is in the class of trigonometric lacunary functions [14,30,31]. Accounting for the properties of the cpn listed in Section 2.2, one obtains a lacunary trigonometric sequence. This is written as

$$|f_N(\rho_1 e^{i\phi})|_{\text{trig}}^2 = 2 \sum_{j=1}^N \gamma_j \cos(k\Delta C(j)\phi), \tag{31}$$

where γ_j is the multiplicity of the j th member of ΔC . Since ΔC consists solely of integers, one directly sees the k -fold symmetry of the cpn-based lacunary functions.

The centered polygonal lacunary functions can be cast in the form of Jacobi theta functions. One has

$$f_N(z) = \sum_{n=1}^N z^{\frac{kn^2 - kn + 2}{2}} = z \sum_{n=1}^N \left(z^{\frac{k}{2}}\right)^{n^2 - n}. \tag{32}$$

Temporarily setting $w = z^{\frac{k}{2}}$ and completing the square gives

$$f_N(z) = z \sum_{n=1}^N w^{(n-\frac{1}{2})^2} w^{-\frac{1}{4}}. \tag{33}$$

Now setting $j = n - 1$ and using symmetry in the dummy index yields

$$f_N(z) = \frac{1}{2}zw^{-\frac{1}{4}} \sum_{j=-(N-1)}^{N-1} w^{(j+\frac{1}{2})^2}. \tag{34}$$

Finally, letting $N \rightarrow \infty$, substituting back in for w , and recognizing the second Jacobi theta function gives

$$f_\infty(z) = \frac{1}{2}zw^{-\frac{1}{4}} \sum_{j=-\infty}^{\infty} w^{(j+\frac{1}{2})^2} = \frac{1}{2}z^{\frac{8-k}{8}} \vartheta_2\left(0; z^{\frac{k}{2}}\right). \tag{35}$$

This connection to the Jacobi theta function brings with it the possibility of employing the rich history of these function in understanding the nature of centered polygonal lacunary sequences. Further, it may provide in-roads for the use of the machinery of modular forms [32] in describing the centered polygonal lacunary systems. These two related directions are not pursued in this work.

Finally, it is noted in passing that subjecting $\mathfrak{L}(C^{(k)}; z)$ to conformal transformations such as dilation, $z \rightarrow e^z$, or linear fractional transformation preserves polish but, of course, breaks rotational symmetry. Particularly interesting are the transformations $z \rightarrow e^z$ and $z \rightarrow \frac{1}{z}$. As is well known, the former maps the natural boundary to the imaginary real axis. The latter maps the natural boundary to itself while exchanging the interior and exterior of the unit disk. Finally, $z \rightarrow ze^{i\theta}$ produces a clockwise rotation through angle θ .

6. Non-Convergence at the Natural Boundary

It is interesting to consider how $|f_N(z)|$ approaches the unit circle along the radial path $z = \rho e^{i\alpha}$. We consider the sequence indexed by N of $\mathfrak{L}(C^{(k)}; \rho e^{i\alpha})$ for values of ρ close to and equal to unity.

6.1. Properties of the Triangular Numbers Modulo n

We list a few of the properties of triangular numbers modulo n which are known. There does not appear to be a convenient reference where these results are all collected. The reader is referred to a ResearchGate paper by the authors with the same title as this subsection for the proofs of the following and many other properties [33].

Lemma 4. *The sequence of triangular numbers mod $2p$ is a $4p$ -cycle. The sequence is symmetric about the midpoint of the $4p$ -cycle.*

Proof. Proof found in reference [33]. \square

Lemma 5. *There is an equal number of even and odd numbers in the first $2p$ members of $4p$ -cycle of Lemma 4.*

Proof. Proof found in reference [33]. \square

Theorem 5. *If $p \neq 2^m$ then the first time 0 reappears is at a position less than the $p - 1$ position.*

Proof. Proof found in reference [33]. \square

Theorem 6. All values appear once and only once in the first p members of the $2p$ -cycle if and only if $p = 2^m$ where m is a positive integer (starting with 0).

Proof. Proof found in reference [33]. □

6.2. Symmetry Angles

Definition 5. Symmetry angle set $\Phi^{(p)}$. $\Phi^{(p)} = \left\{ \frac{\pi}{kp} (T \bmod 2p) \right\}$.

Lemma 6. The size of $\Phi^{(p)}$, $|\Phi^{(p)}|$, is independent of k and is finite.

Proof. Since $\frac{\pi}{kp}$ multiplies $t \bmod 2p$, then $|\Phi^{(p)}|$ is determined only by $|T \bmod 2p|$, which is independent of k . Further, by Lemma 4, $T \bmod 2p$ is a $4p$ -cycle. Hence, $|T \bmod 2p|$ is finite and thus $|\Phi^{(p)}|$ is as well. □

Theorem 7. For all $N > 2p$,

$$f_N \left(e^{\frac{i\pi}{kp}} \right) = \sum_{j=1}^{|\Phi^{(p)}|} M_j e^{i\phi_j}, \tag{36}$$

where M_j is the overall number of times ϕ_j is reached in the set $\{T(n) \bmod 2p\}$ for $n = 1$ to $N - 1$.

Proof. Beginning with

$$\begin{aligned} f_N \left(e^{\frac{i\pi}{kp}} \right) &= \sum_{n=1}^N \left(e^{\frac{i\pi}{kp}} \right)^{C^{(k)}(n)} = \sum_{n=1}^N e^{\frac{i\pi}{kp} \cdot \frac{kn^2 - kn + 2}{2}} \\ &= \sum_{n=1}^N e^{\frac{i\pi}{kp}} e^{\frac{i\pi}{p} \frac{n^2 - n}{2}}. \end{aligned} \tag{37}$$

Now, resetting the dummy summation index to $n \rightarrow n - 1$,

$$f_N \left(e^{\frac{i\pi}{kp}} \right) = \sum_{n=0}^{N-1} e^{\frac{i\pi}{kp}} e^{\frac{i\pi}{p} \frac{n^2 + n}{2}} = \sum_{n=0}^{N-1} e^{\frac{i\pi}{kp}} e^{\frac{i\pi}{p} T(n)}. \tag{38}$$

Now, the number $e^{\frac{i\pi}{p} T(n)}$ is periodic, as it depends on $T(n) \bmod 2p$. By Lemma 4 $T \bmod 2p$ is a $4p$ -cycle and defines the symmetry angle set. Thus,

$$f_N \left(e^{\frac{i\pi}{kp}} \right) = \sum_{j=1}^{|\Phi^{(p)}|} M_j e^{i\phi_j}. \tag{39}$$

□

Definition 6. Multiplier set $M^{(p)}$. The set of coefficients, M_j , for the function in Equation (36).

The pair of sets $\{M^{(p)}, \Phi^{(p)}\}$ can then be used to represent the limit value of $f_N \left(e^{\frac{i\pi}{kp}} \right)$ via the obvious association with the equation above.

As one might expect, the plots of the sequence of values at $z = z_0$, $\{f_N(z_0)\}$ are dependent on angle, α . Certain special angles are those consistent with the rotational symmetry of $|f_N(z)|$, namely the first, second, etc., symmetry angles. Figure 7 shows the convergence behavior of the real (blue) and imaginary (red) parts of $f_N(z)$ along the first and second symmetry angle for the example of $\mathcal{L}(C^{(3)}; z)$. Limit values at $\rho = 0.9, 0.99, \dots, 0.99999, 1$ for N ranging from 2 to 150 are shown. As $\rho \rightarrow 1$

convergence slows and finally at $\rho = 1$ there is not a convergent limit point. It is the case, however, that the limit value depends on N in a bounded way.

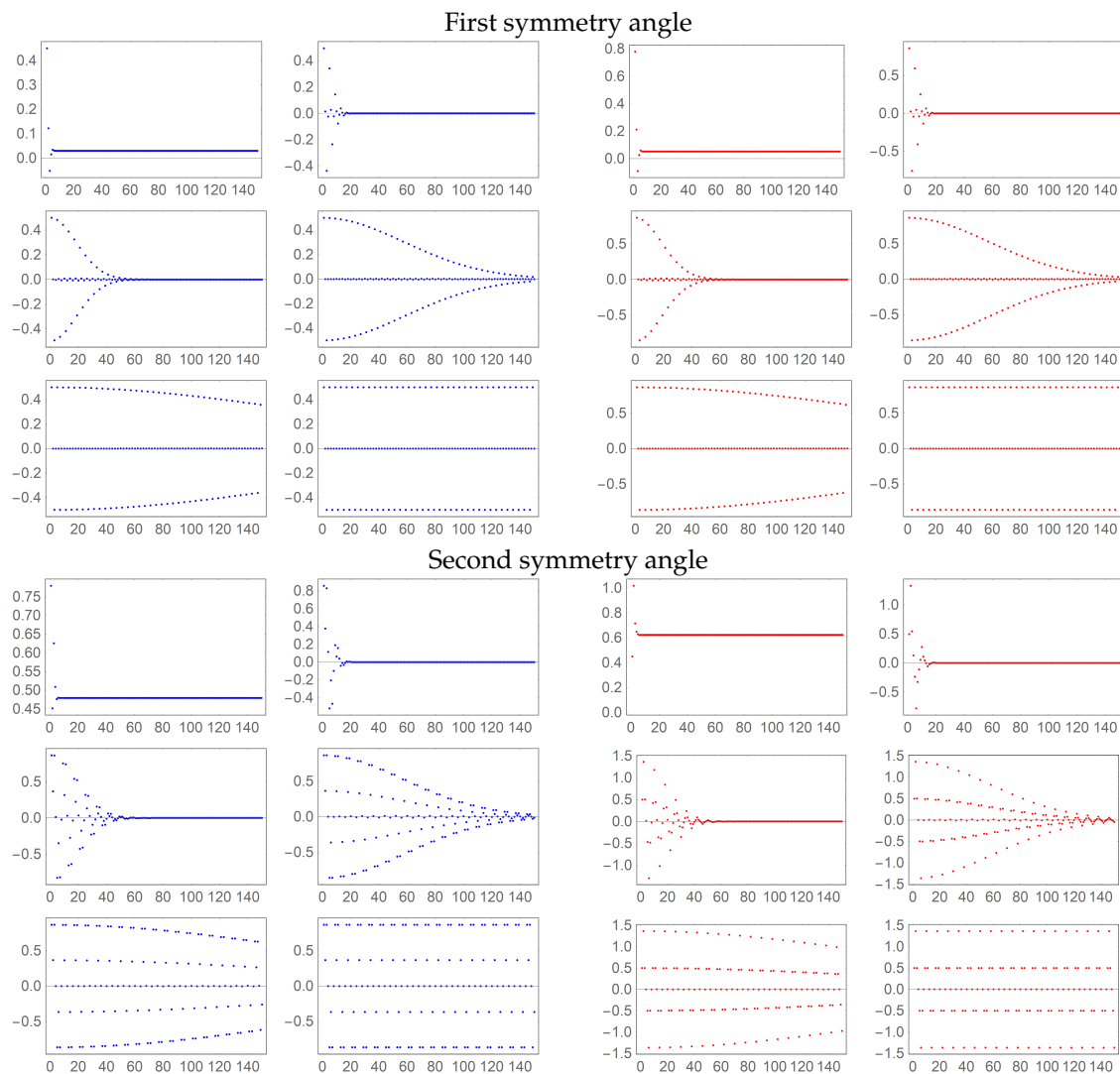


Figure 7. Top set, first symmetry angle: Limit value of $\mathfrak{L}(C^{(3)}; \rho e^{\frac{i\pi}{3}})$ (real part, blue; imaginary part, red) at $\rho = 0.9, 0.99, 0.999, 0.9999, 0.99999, 1$ as a function of N . Bottom set, second symmetry angle: Limit value of $\mathfrak{L}(C^{(3)}; \rho e^{\frac{i\pi}{6}})$ (real part, blue; imaginary part, red) at the same values of ρ as above.

For example, consider the paths $z = \rho e^{\frac{i\pi}{l}}$, $l = 3, 6, 9, \dots$ for $\mathfrak{L}(C^{(3)}; z)$. For $\rho = 0.9$, the sequence quickly converges with respect to N to a limit value. But as ρ approaches unity the convergences slows. Finally, at $\rho = 1$ the sequence does not converge. For the special angles the sequence is bounded. Indeed for the first symmetry angle the sequence is

$$\mathfrak{L}(C^{(k)}; e^{\frac{i\pi}{k}}) = \{ \dots, -e^{\frac{i\pi}{k}}, 0, e^{\frac{i\pi}{k}}, 0, -e^{\frac{i\pi}{k}}, 0, e^{\frac{i\pi}{k}}, \dots \}. \tag{40}$$

and along the second symmetry angle the sequence is

$$\mathfrak{L}(C^{(k)}; e^{\frac{i\pi}{2k}}) = \{ \dots, 0, -e^{\frac{i\pi}{2k}}, -e^{\frac{i\pi}{2k}} - e^{-\frac{i\pi}{k}}, -e^{\frac{i\pi}{2k}}, 0, e^{\frac{i\pi}{2k}}, e^{\frac{i\pi}{2k}} + e^{-\frac{i\pi}{k}}, e^{\frac{i\pi}{2k}}, 0 \dots \}. \tag{41}$$

In general, the sequence is unbounded for angles, α , that do not coincide with integer fractions of π . However, the sequence of limit values of $f(z)$ at the natural boundary along the set of p th symmetry

angles has some elaborate structure and deep connection to the triangular numbers. The N th member, S_N , of the sequence of limiting values along the p th symmetry angle is part of a $4p$ -cycle of values. This cycle begins immediately at the $N = 1$ level and has the following structure. Every term contains a simple factor of $\sqrt[p]{-1}$ which is the only factor that carries k dependence. Thus, $S_N = \sqrt[p]{-1}\sigma_N$. The σ_N follow a $4p$ -cycle that has its own substructure. Let $M = N \bmod 4p$ be the index of the $4p$ -cycle and let $\hat{\sigma}_M$ represent $\sigma_N \mapsto \hat{\sigma}_N$ under the mod. The structure of the sequence of $\hat{\sigma}_M$ values is $\{\hat{\sigma}_1, \hat{\sigma}_2, \dots, \hat{\sigma}_p, \hat{\sigma}_{p-1}, \dots, \hat{\sigma}_0, -\hat{\sigma}_1, \dots, -\hat{\sigma}_p, -\hat{\sigma}_{p-1}, \dots, -\hat{\sigma}_1, \hat{\sigma}_0\}$, thus only p , rather than $4p$, distinct $\hat{\sigma}_M$ must be determined. These values are

$$\begin{aligned} \hat{\sigma}_0 &= 0 \\ \hat{\sigma}_1 &= 1 \\ \hat{\sigma}_{i+1} &= \sum_{j=0}^i (-1)^{\frac{T(j)}{p}}, \end{aligned} \tag{42}$$

where $2 \leq i \leq p - 1$. Note: $\hat{\sigma}_0$ is really $\hat{\sigma}_{p+1} = 0$ but it proves convenient to limit the run of i to p and define $\hat{\sigma}_0 = 0$.

6.3. Theorems on the Limit Values along Symmetry Angles

The above analysis is made a bit more rigorous with the following set of lemmas and theorems.

Theorem 8. The members, S_N , of the sequence of limiting values generated by $f_N \left(e^{\frac{i\pi}{kp}} \right)$ are of the form $S_N = \sqrt[p]{-1}\sigma_N$ where σ_N is independent of k .

Proof. Write

$$\begin{aligned} S_N &= e^{\frac{i\pi C^{(k)}(1)}{kp}} + e^{\frac{i\pi C^{(k)}(2)}{kp}} + e^{\frac{i\pi C^{(k)}(3)}{kp}} + \dots \\ &= e^{\frac{i\pi}{kp}} \left(e^{\frac{i\pi C^{(k)}(1)-1}{kp}} + e^{\frac{i\pi C^{(k)}(2)-1}{kp}} + e^{\frac{i\pi C^{(k)}(3)-1}{kp}} + \dots \right). \end{aligned} \tag{43}$$

Now, by Lemma 2 and by $e^{\frac{i\pi}{kp}} = \sqrt[p]{-1}$,

$$S_N = \sqrt[p]{-1} \left(e^{\frac{i\pi T(0)}{p}} + e^{\frac{i\pi T(1)}{p}} + e^{\frac{i\pi T(2)}{p}} + \dots \right), \tag{44}$$

where $T(0) = 0$. This proves the theorem because k dependence is in the first factor only. \square

Theorem 9. Equation (42) holds.

Proof. By Theorem 8 $S_N = \sqrt[p]{-1} \left(e^{\frac{i\pi T(0)}{p}} + e^{\frac{i\pi T(1)}{p}} + e^{\frac{i\pi T(2)}{p}} + \dots \right)$. Each term, $e^{\frac{i\pi T(m)}{p}} = e^{\frac{i\pi}{p}(T(m) \bmod 2p)}$ by the cyclic nature of e^{ix} . By Lemma 4, $T(m) \bmod 2p$ is a member of symmetric $4p$ -cycle. Then by Lemma 5 there is an equal number of even and odd terms in the first $2p$ members of the $4p$ -cycle. Thus $S_{N=m2p} = 0$, where m is an integer. And, by symmetry, $S_{N=m4p} = 0$. Thus one need consider only the $4p$ member set $\{\hat{\sigma}_M\}$ and

$$\hat{\sigma}_i = e^{\frac{i\pi T(0)}{p}} + e^{\frac{i\pi T(1)}{p}} + e^{\frac{i\pi T(2)}{p}} + \dots + e^{\frac{i\pi T(i)}{p}}. \tag{45}$$

Using $e^{\frac{i\pi T(m)}{p}} = e^{\frac{i\pi}{p}(T(m) \bmod 2p)}$ and $e^{i\pi} = -1$ yields Equation (42). \square

6.4. Fibered Space for Identification of Equivalence Classes

A convenient way to deal with the emerging $4p$ -cycles discussed above is through the use of a primitive fiber bundle. The adjective “primitive” is used to alert the reader this bundle lacks manifold structure that is attendant when one typically thinks of a fiber bundle [34]. The bundle will be constructed as follows.

The base space will be the unit circle in the complex plane, $S^1 = \{|z| = 1\}$. In the base space, the symmetry angle set, defined above, is identified: $\Phi^{(p)} \in S^1$. The typical fiber is the set of positive integers, \mathbb{Z}^+ . Copies of the typical fiber are attached to the base space at the points $\Phi^{(p)}$. Collectively the bundle is $\mathfrak{B}^{(p)} = \{B^{(p)}, S^1, \mathbb{Z}^+, \Phi^{(p)}, \hat{\pi}\}$, where $B^{(p)}$ is the total space, and $\hat{\pi}$ is the projection from $B^{(p)}$ to $\Phi^{(p)} \in S^1$ such that $\hat{\pi}^{-1}$ maps to the typical fiber and $\hat{\pi}^{-1}(\phi_i) = M_i$ where is $M_i \in M^{(p)}$, the multiplier set.

A cross-section (simply referred to as section hereafter), $\Sigma(f_N(z))$, on $\mathfrak{B}^{(p)}$ can conveniently represent limiting values at the natural boundary along angle α_i of $f_N(z)$. This is illustrated for $\mathcal{L}(C^{(3)}; z)$ for $p = 1, 2$, and 4 in Figure 8. The sections reveal the basic structure of what makes up the limit values of $f_N(z)$. The $4p$ -cycle manifests in the number of distinct sections for a given p ; 4, 8, and 16 for the example in Figure 8. Further the $2p$ number of $\phi_i \in \Phi^{(p)}$ appear in the example as well. Note, however, that this example shows non-degenerate cases. The degenerate case is addressed below. The section is a graphical way to represent $\{M^{(p)}, \Phi^{(p)}\}$ for a particular N . The collection of all sections on $B^{(p)}$ then represent the entire lacunary sequence for $f_N(z)$.

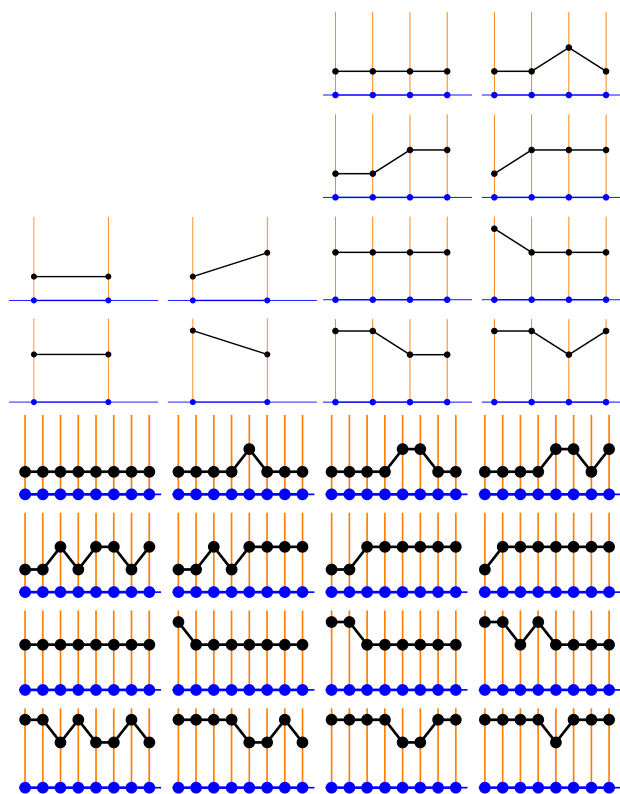


Figure 8. Sections for the example of $\mathcal{L}(C^{(3)}; z)$ for $p = 1$ (top left), $p = 2$ (top right), and $p = 4$ (bottom). The base space is shown as a blue line and $\Phi^{(p)}$ as blue points on that line. The fibers are shown as orange and the sections are the black dots. The black lines are simply to help the eye when comparing sections.

The sections also provide a convenient way to define equivalence classes. Sections having the same shape form an equivalence class. An example of this is shown in Figure 9 where the fourth section in the set for $p = 4$ of $\mathcal{L}(C^{(3)}; z)$ (bottom set in Figure 8) is used as a concrete example. There

is an infinite number of repetitions of similar sections for every $f_{3+16m}, m \geq 0 \in \mathbb{Z}^+$ (the 16 comes from the $4 \cdot (p = 4) = 16$ cycle). This collection constitutes a single equivalence class, which for this example is $\hat{\sigma}_3$.

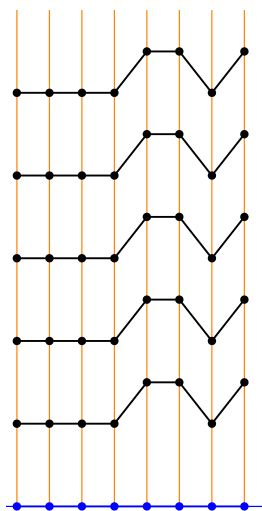


Figure 9. Some of the infinite number of similar sections to that of the fourth section in the set for $p = 4$ of $\mathcal{L}(C^{(3)}; z)$ (bottom set in Figure 8). This forms the equivalence class $\hat{\sigma}_3$.

The first degenerate case occurs when $p = 3$. This is shown in Figure 10, where one of the 12 sections is used as an illustrative example. For degenerate cases, pairs of the $2p$ members of $\Phi^{(3)}$ coalesce, leaving fewer distinct points in the base space. This results in those points having multiplier values that are twice that of the non-coalesced points. The following conjecture is noted in passing and without proof. The only non-degenerate cases occur when $p = 2^n$.

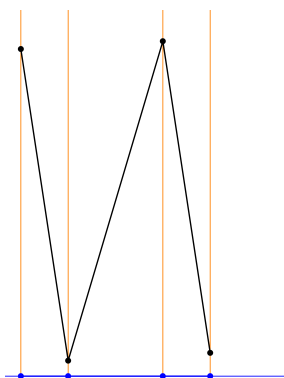


Figure 10. The $\hat{\sigma}_2$ section for the $p = 3$ case. For this degenerate case, two pairs of the six $2p$ members of $\Phi^{(3)}$ coalesce, leaving four distinct points in the base space (blue dots). This results in those points having multiplier values that are twice that of the non-coalesced points.

Another virtue of the fiber bundle treatment is that the k -independent features are emphasized. The same general sections (and, thus, equivalence classes) will appear regardless of k . The different k will change the numerical values of the $\phi_i \in \Phi^{(p)}$ nonetheless, the sections look similar. This is the fiber manifestation of $S_N = \sqrt[k]{-1}\sigma_N$. Figure 11 shows the same section for $k = 3$ and $k = 6$. In each case $p = 2$.

The equivalence classes of sections can themselves be partitioned into equivalence classes based simply on their shape. That is, sections with the same number of offset points will give the same value for f_N . The null class, which corresponds to $\hat{\sigma}_0$, is where all the points in the section are at the same value (all M_j are equal). The other sections then have one or more points at a different value than the

null class. The $p = 4$ case in Figure 8 (bottom panel) can serve as a handy concrete case. The first and ninth sections are members of the null class. The second and the tenth show one point above the remainder of the section. These two points have equivalent values. The seventh and the sixteenth sections each have one point below the remainder of the section. These have equal values. The case of one point up and one point down are equivalent in absolute value. Thus, at the $|f_N|$ level all four sections are in the same equivalence class.

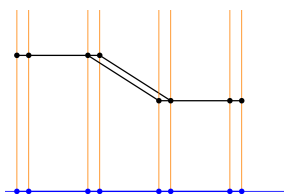


Figure 11. A comparison of the $\hat{\sigma}_6$ section for the case of $k = 3$ and $k = 6$ and $p = 2$. One notes that the general shape is the same although the numerical values of the ϕ_i change. All sets of sections exhibit this type of similarity across values of k . Increasing k shifts the fiber positions to the left.

Likewise, the two points up/down form a class, as do the three point up/down form a class. There are only two four point up/down sections (fifth one and thirteenth one) in the last class. It is noteworthy that at the $|f_N|$ level the sum of each individual equivalence class is zero. For example, adding the values of the two one point up sections to the two one point down sections equals zero.

The virtue of the primitive fiber bundle approach is that it graphically exposes some of the structure of the centered polygonal lacunary sequences. Clearly, the set of symmetry angles offer a special path of approach, $z = \rho e^{i\pi/kp}$, to the natural boundary. Further, the cyclic nature of the sequences suggests a refining definition for the associated lacunary function. This refinement is

$$f_{\bar{N}} \left(\rho e^{i\pi/kp} \right) = \sum_{n=1}^{4p\bar{N}} \left(\rho e^{i\pi/kp} \right)^{C^{(k)}(n)}. \tag{46}$$

One might be tempted to consider this as perhaps a way to perforate the natural boundary and analytically continue outside of it. Indeed, the limit value at the natural boundary of $f_{\bar{N}} = 0$ for all \bar{N} . However, as the \bar{N} tends to infinity, singularities arise infinitesimally close to the special path. Consequently, the radius of convergence for the point on the special path at the natural boundary shrinks to zero. And analytic continuation is pinched-off.

Another interesting consideration in the context of the primitive fiber bundles is to consider the limit $p \rightarrow \infty$. Here, the number of points in $M^{(p)}$ goes to infinity (albeit relatively slowly). Further, the points become dense on S^1 . Consequently, the number of section equivalence classes also approaches infinity and, hence, the cyclic nature of the lacunary sequence is lost.

The primitive fiber bundle approach graphically exposes some of the structure of the centered polygonal lacunary sequences. Clearly, the set of symmetry angles offers a special path of approach to the natural boundary, which gives rise to the p -sequences.

It is helpful to reduce the consideration of the full set of sections for a given p value down to a single fiber position diagram which is simply a graphical representation of the base space, S^1 , which is represented by a grey circle. The circle is partitioned evenly with grey dots appearing at every π/p . The fiber positions are represented by blue dots that eclipse the grey dots at points where the fibers join the base space. Examples of fiber position diagrams are shown in Figure 12 and utilized in the following section. But first, two symmetry theorems are listed:

Theorem 10. *If position d_i is occupied by a fiber so is the antipodal position d_{i+p} . Fiber position diagrams have inversion symmetry.*

Proof. The fiber positions coincide with the values of the triangle numbers modulo p . By Lemma 4, the sequence is symmetric about the midpoint of the $2p$ -cycle. When cast onto S^1 as with the fiber diagrams, this means points occupied in the upper semi-circle and lower semi-circle will coincide antipodally. This completes the proof. \square

Theorem 11. *Fiber position diagrams are at least 2-fold rotationally symmetric. (One says it has \hat{C}_2 symmetry.)*

Proof. The fiber diagrams lie in a plane and inversion symmetry is equivalent to \hat{C}_2 in the plane. \square

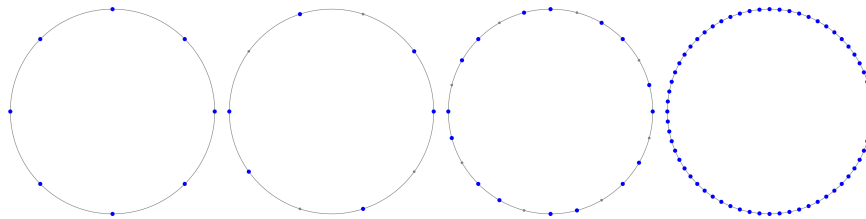


Figure 12. Examples of fiber position diagrams for the cases (left-to-right) of $p = 4, 5, 12, 32$. The blue dots are the positions of the fibers on the base space and the grey dots represent equal divisions of the circle in units of π/p . For example the bottom panel of Figure 8 corresponds to the first diagram. The unit cell size is (left-to-right) $1/8, 1/2, 1/8, 1/64$. The saturation value is (left-to-right) $1, 3/5, 2/3, 1$.

7. Structure of Limit Value Sequences

The fiber position diagrams offer a nice way of visualizing two important definitions that help characterize the structure of the limit values of the centered polygonal lacunary sequences along the symmetry angles.

7.1. Degree of Saturation

Definition 7. *Saturation.* The degree of saturation, s , of a p -sequence is the percent overlap of the fiber positions and the partition points at π/p .

The saturation is easily identified from the fiber position diagrams. By way of example, consider the fiber position diagrams shown in Figure 12. For the case of $p = 4$, all eight partition points are covered by fiber positions. Thus the saturation value is $s = 1$. For the case of $p = 5$, not all the partition points are covered by fiber positions. In fact, only $3/5$ of them are covered and hence $s = 3/5$. Likewise, $s = 2/3$ and $s = 1$ for the cases of $p = 12$ and $p = 32$, respectively, which is immediately read from the diagram. The following corollary is immediate from Theorem 6.

Corollary 2. *The saturation, $s = 1$, if and only if $p = 2^m$ for positive integer m .*

The top right panel of Figure 13 shows the saturation data for $p = 1$ through 128. Corollary 2 is readily evident. There is an interesting preponderance of p -sequences having approximately $s = 1/2$. This is the subject of on-going investigation.

The bottom right panel of Figure 13 shows the number of fiber positions as a function of p . It is not surprising that is is very much related to the data in the top right panel. Only the cases of $p = 2^m$ lie along the $s = 2p$ line. Almost all of the values lie between the $s = p$ and $s = p/2$ lines. As stated above the number of fiber positions is equal to the number of terms in the sum representing the lacunary p -sequence.

7.2. Unit Cell Size

An important definition borrows its name from crystallography.

Definition 8. Unit cell size, u . The unit cell of a fiber position diagram is the smallest repetitive portion of the diagram.

It is noted that the unit cell is very much related to the rotational symmetry, \hat{C}_n , of the fiber position diagram (the reader is cautioned that \hat{C}_n is not connected to the cpns in spite of the similarity of symbol). Indeed, $\hat{C}_n = \hat{C}_{\frac{1}{u}}$.

As with degree of saturation, the unit cell size is immediately read from the fiber position diagram. Momentary inspection of those diagrams shown in Figure 12 shows a unit cell value of $u = 1/8, 1/2, 1/8, 1/64$ from left-to-right, respectively. There are a few corollaries and theorems associated with the unit cell.

Corollary 3. $u = \frac{1}{2^p}$, if and only if $p = 2^m$ for positive integer m .

Proof. This follows from corollary 2 and the definitions of partition points and the unit cell. □

Theorem 12. The allowed values of u are $u = \frac{1}{2^m}$, for positive integer m .

Proof. This follows from Theorem 11. If the fiber position diagram is to maintain the \hat{C}_2 symmetry, the next lowest symmetry must be \hat{C}_4 because \hat{C}_3 symmetry would violate the \hat{C}_2 symmetry. Now, the next lowest symmetry must be \hat{C}_8 since $\hat{C}_5, \hat{C}_6,$ and \hat{C}_7 would violate \hat{C}_4 . This reasoning continues ad infinitum and thus concludes the proof. □

Theorem 13. $u = 1/2$, for p odd.

Proof. The proof follows that of Theorem 12. In order to maintain \hat{C}_2 symmetry, there cannot be \hat{C}_{odd} symmetry. In order for the unitcell to have any greater symmetry than \hat{C}_2 , that symmetry must be \hat{C}_{even} in which case the $\frac{2^p}{4}$ position on S^1 must be available. But p is taken to be odd, so $\frac{2^p}{4}$ is not an integer, hence a contradiction results. This completes the proof. □

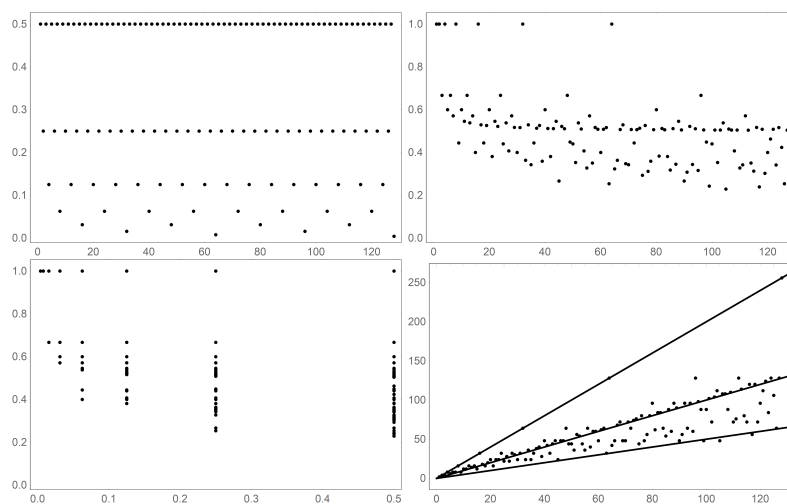


Figure 13. Several plots of data sets exposing some of the structure of the limit values of the centered polygonal lacunary sequences. These data are independent of k and thus hold for all centered polygonal lacunary functions at once. In all cases, the data are plotted as a function of p from $p = 1$ to 128 (the horizontal axis). The top left panel shows the unit cell size as a function of p from $p = 1$ to 128. The top right panel shows the saturation value versus p from $p = 1$ to 128. The bottom left panel shows the saturation as a function of unit cell size. The bottom right panel shows the number of fiber positions on the base space.

7.3. Autocorrelation

While the fiber position diagrams readily reveal a number of aspects of the structure of centered polygonal lacunary p -sequences, other aspects are too subtle to be read graphically by simple inspection. To address this, autocorrelations can be associated with each fiber position diagram. The autocorrelations are defined in the typical way. That is, if one of the $\frac{\pi}{p}$ (grey dot) positions on S^1 is occupied by a fiber, then that position is assigned a value of 1. Otherwise it is assigned a value of 0. This collection is $f(j)$, then

$$A(\tau) = \sum_{j=0}^{2p} f(j)f(j + \tau). \tag{47}$$

Figure 14 shows four representative examples of autocorrelations for some high p value cases. The collection of examples shown in Figure 14 does well to illustrate the ability of the autocorrelation function to expose distinguishing features of the fiber position diagrams. Aside, perhaps, from some noticeable differences in the clustering of the fiber positions, the fiber position diagrams shown in the figure are rather nondescript and difficult to distinguish from one another. On the contrary, their associated autocorrelation graphs are very distinctive.

Primes appear as a single peak with a 2:1 peak to background ratio; $p = 59$ and 61 in this case. But even further, primes of the form $4n - 1$ (non-Pythagorean) have a constant background background while the Pythagorean primes (those of the form $4n + 1$) have a noisier background. In the case of non-Pythagorean primes, this means that the fiber positions are such that when displaced by a non-zero value of τ exactly half coincide.

The value of $p = 56 = 2^3 \cdot 7$ involves a single odd prime and it displays a very regular pattern which is related to its unit cell value ($u = 1/16$ for $p = 56$). The number of peaks in the $-\pi/2$ to $\pi/2$ is $\frac{1}{2u}$. The peak to background ratio is 2:1 here as well. The autocorrelation for the case of $p = 60 = 2^2 \cdot 3 \cdot 5$ has more structure because two different odd primes are factors. In a sense, the autocorrelation captures a beat pattern between the contribution from the 3 and the contribution from the 5. In general, fiber position diagrams for p values that involve many different primes factors have more complex beat structure.

The fiber position diagrams for p values that have only one odd prime but that which is raised to a power (example not shown) have a similarly clean, regular structure to that of example seen with $p = 56$. The difference is that the individual peak heights vary in amplitude.

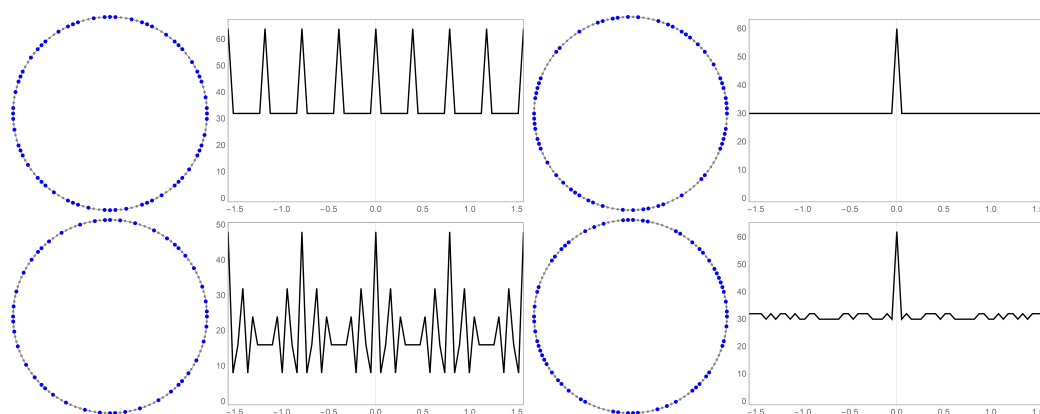


Figure 14. Fiber position diagrams and their corresponding autocorrelations for $p = 56$ (top left), $p = 59$ (top right) which is non-Pythagorean, $p = 60$ (bottom left), and $p = 61$ (bottom right), which is Pythagorean. It is difficult for the eye to discern subtle details in the structure of the fiber position diagrams, especially for large p values. The autocorrelations, however, are quite distinct for these four similar cases.

8. Relation to Lacunary Trigonometric Systems

The centered polygonal lacunary functions give rise to centered polygonal lacunary trigonometric systems by considering the function around the natural boundary. That is, $\mathfrak{L}(C^{(k)}; e^{i\phi})$. These lacunary trigonometric systems have interesting structure that includes a fractal-like scaling feature.

Figure 15 shows some of the important features of the centered polygonal lacunary trigonometric systems. The top row of graphs are of two members of $|\mathfrak{L}(C^{(4)}; e^{i\phi})|$, for relatively low N values. The top left graph is of $f_{12}(e^{i\phi})$ and the top right graph is of $f_{25}(e^{i\phi})$. Although these graphs already appear rather messy, one can still notice regularity. The most prominent are the spikes at $\phi = 0, \pm\frac{\pi}{2}, \pi$. The value of $f_N(e^{i\phi})$ is equal to N at these angles. This is because these are the angles where all the N terms are adding in-phase. The middle left graph shows a blow-up around $\phi = 0$ for $N = 100$. The maximum value is indeed 100. Further, the function is much less jagged near the spike as compared with the wings. Also, one sees clearly distinct regions in the wings.

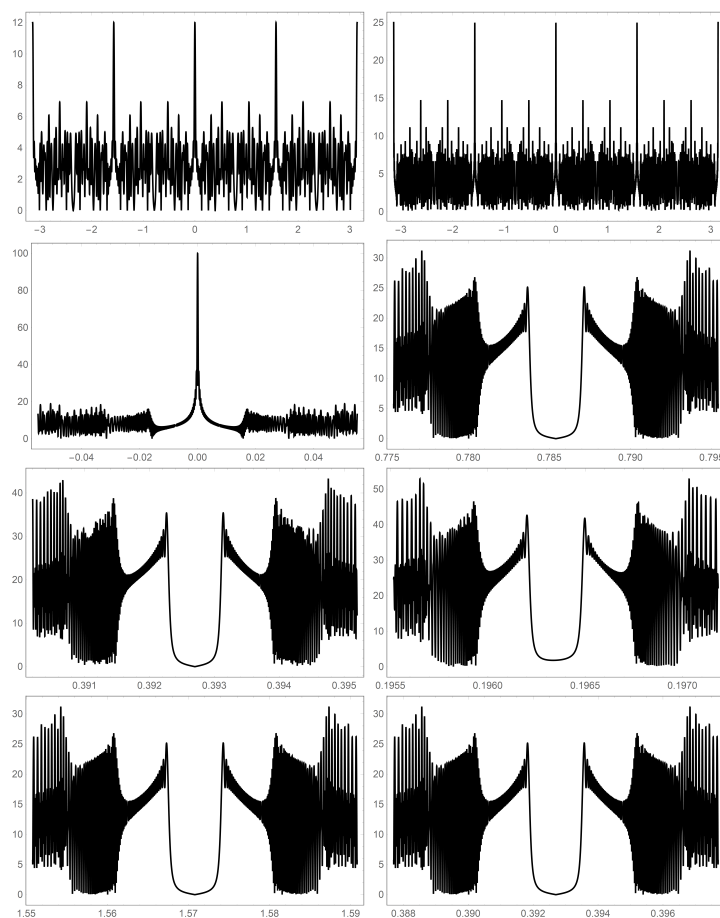


Figure 15. The lacunary trigonometric system obtained from $\mathfrak{L}(C^{(4)}; z)$ by setting $z = e^{i\phi}$. The top row compares the full range $-\pi < \phi < \pi$ for the case of $N = 12$ (left panel) and $N = 25$ (right panel). The left panel in the second row shows a blow-up around $\phi = 0$ and $N = 100$. The right panel in the second row and the two panels in the third row expose the scaling property of the system. Note the similarity of the graphs. The right panel in the second row is at the first symmetry angle, $\phi = \frac{\pi}{4}$, with $N = 250$ and a plot range of 0.02. The left panel in the third row is centered at the second symmetry angle, $\phi = \frac{\pi}{8}$, now with $N = 500$ and a full plot domain of a fourth of that of the second row right panel. The right panel in the third row is centered at the third symmetry angle, $\phi = \frac{\pi}{12}$. Here, $N = 750$ and a full plot domain is one-twelfth that of the second row right panel. The bottom row shows scaling similarity across different values of k . The first symmetry angle is shown. The bottom left panel shows the case of $\mathfrak{L}(C^{(2)}; z)$ and the right panel shows the case of $\mathfrak{L}(C^{(8)}; z)$. In both cases $N = 250$. For the $k = 2$ case, the range is twice that for the $k = 4$ case, while for the $k = 8$ case, the range is half that of $k = 4$.

The remaining five graphs in Figure 15 expose a fractal like scaling property of these systems. These graphs concentrate on regions near the symmetry angles which are troughs. As with the spikes, the immediate region of the trough is much less jagged than the surrounding wings.

The graphs are respectively centered at the first ($\phi = \frac{\pi}{4}$), second ($\phi = \frac{\pi}{8}$), and third ($\phi = \frac{\pi}{12}$) symmetry angles of $\mathcal{L}(C^{(4)}; z)$. If one scales the domain by a factor of $\frac{1}{k^p}$ and scales the number of terms in f by a factor of p then one sees identical graphs. The scaling behavior with p provides insight on how the singularities encroach upon the symmetry angles as they move towards zero (i.e., as $p \rightarrow \infty$). The trough around the p th symmetry angle closes as $1/p$ for a set value of k . For scaling across different values of k , holding N constant and scaling the range by $\frac{k_1}{k_2}$ results in identical-looking graphs.

$|\mathcal{L}(C^{(k)}; e^{i\phi})|$ also exhibit scaling similarity as a function of N . Again the example of $|\mathcal{L}(C^{(4)}; e^{i\phi})|$ is considered and shown in Figure 16. Here, the region around the first symmetry angle is shown of $\alpha_1 = \frac{\pi}{4}$. The panels in the figure progress as $N = 50, 100, 200, 300$ and the domains decrease as $\pm 0.04, \pm 0.02, \pm 0.01, \pm 0.00667$ (i.e., as $1/N$). Clearly, a quasi-self-similarity is present in these data. One does not expect exact self-similarity in this case because increasing N gives rise to high frequency terms not present in lower N values. Thus, one observes higher frequency fluctuations in the wings of the graph and steeper walls of the central trough as N increases.

The scaling behavior with N gives insight on how the singularities enclose around the point on the natural boundary corresponding to a symmetry angle. One can see that the trough around a symmetry angle closes as $1/N$.

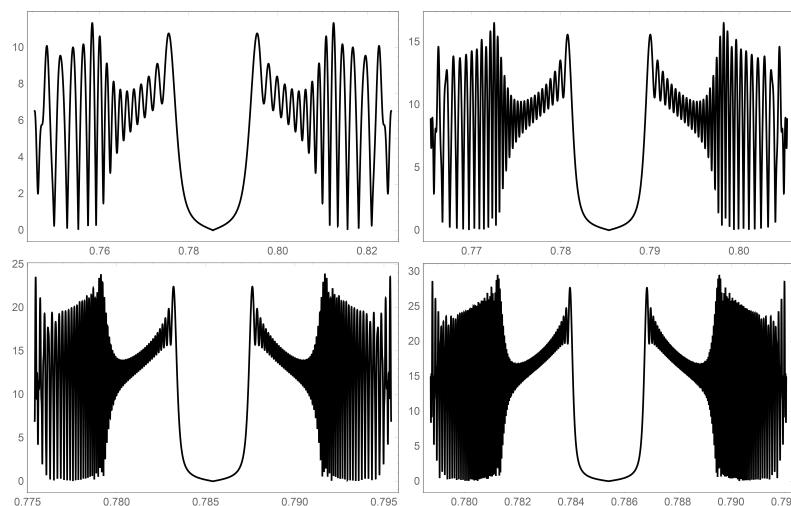


Figure 16. The scaling behavior with N of lacunary trigonometric system obtained from $|\mathcal{L}(C^{(4)}; z)|$ by setting $z = e^{i\phi}$. The four panels show the region around the first symmetry zero ($\frac{\pi}{4}$). Quasi-self-similarity is seen as N changes: top left, $N = 50$; top right, $N = 100$; bottom left, $N = 200$, bottom right, $N = 300$. The domain size scales as $1/N$.

9. Radial Functions along Special Angles

Given the above discussion, the natural choice for N when plotting the radial function along the p th symmetry angle is some multiple of $4p$. This will ensure the function is zero at that natural boundary. The radial function is displayed in a couple of ways in Figure 17. The left panel is a plot of $|f_N(\rho e^{\frac{i\pi}{kp}})|$ for $k = 3$ and $p = 1$ through 10. The right panel shows a “heat map” of the same functions, except now for $p = 1$ through 20 superimposed on $|f_N(z)|$. The graphs skew towards the natural boundary as p increases. Further, the maximum value of the function increases with increasing p as well. It turns out the maximum value asymptotically follows a simple function of p : $y(p) = \sqrt{\frac{p}{2}}$, as shown in Figure 18.

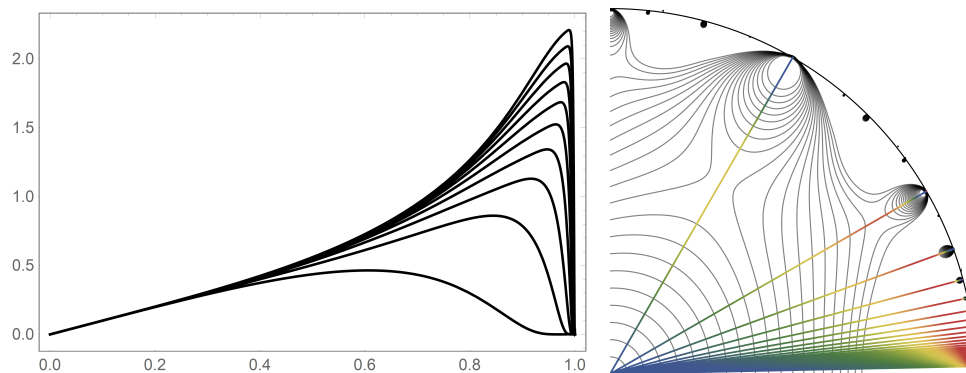


Figure 17. Radial plots of $|\mathcal{L}(C^{(3)}; e^{i\pi/3p})|$ for various values of p . The right panel shows the first 10 symmetry angles. The top curve, which is also most skewed to the right, corresponds to $p = 10$ whereas the bottom curve corresponds to $p = 1$. It is true, in general, that $|f_N|$ along the symmetry angles exhibits an increasing maximum value with increasing p and that the position of the maximum migrates towards the unit circle. The right panel displays $|f_N|$ as “heat map” (blue—low value, red—high value) superimposed on the contour plot of $|f_N(z)|$.

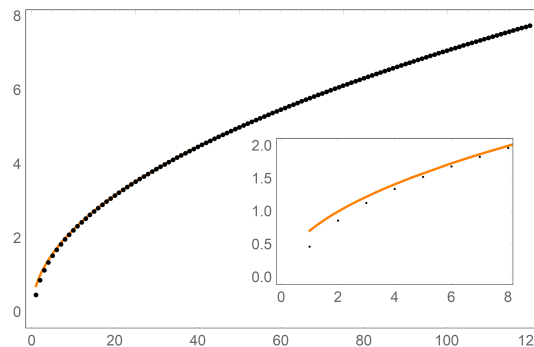


Figure 18. Maximum of the radial function along the p th symmetry angles. The maximum values (black dots) closely follow $y = \sqrt{\frac{p}{2}}$ (orange curve). The inset shows that for low values of p there is deviation from $y = \sqrt{\frac{p}{2}}$.

The cyclic nature of the limit values allow for a convenient approximation to the radial functions along the symmetry angle. The first time the limit value at the natural boundary vanishes occurs when $N = 2p$. Truncation of the lacunary series at this point will be referred to as the *first convergence approximate*. Examples for $|\mathcal{L}(C^{(2)}; e^{i\pi/2p})|$ and $|\mathcal{L}(C^{(4)}; e^{i\pi/4p})|$ are shown in Figure 19. The first convergence approximate for the case of $p = 1$ consists of only two terms and yet it captures the small ρ behavior very well. This improves as k increases (and still consists of only two terms). The first convergence approximate for the case of $p = 3$ contains six terms. The approximation is very good nearly up to the position of the peak of the function. Despite the good approximation at low values of ρ and the fact that the approximate is forced to vanish at the natural boundary, deviation occurs as one approaches the natural boundary. Unfortunately, this is the most interesting part of the function.

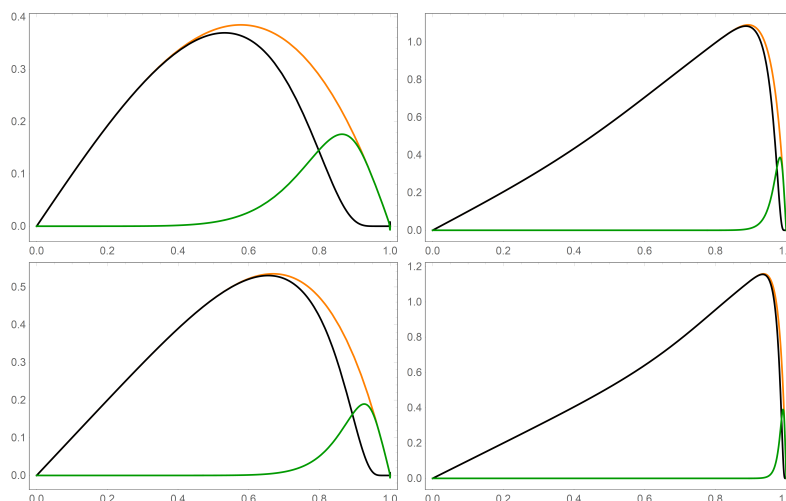


Figure 19. Illustration of the first convergence approximates to the radial function. The top row shows the case of $k = 2$ for $p = 1$ (left) and $p = 3$ (right) and the bottom row shows the case of $k = 4$ for $p = 1$ (left) and $p = 3$ (right). The approximation is exceptional up to the peak maximum in all cases. Beyond the peak maximum, the approximation improves both when k increases and when p increases. The black curve is the “exact” case, f_{40p} and the orange is the first convergence approximate. The green is the residual.

10. Some Numerical Analysis

Several aspects of centered polygonal lacunary functions are explored numerically in this section. These include a concept referred to here as “contour budding,” a scaling relation between different values of k and integration along a symmetry angle.

10.1. Contour Budding

Inspection of the contour plots of $|f_N(z)|$ reveal simple closed rectifiable orientable curves in the unit disk determined by the level set value. The plots also prominently reveal the first symmetry zeros (as well as the second symmetry zeros, albeit less prominently). The set of contours shown within the plots exhibits a separatrix that separates the domain D_0 in which the origin and the first symmetry zeros are simply connected (in the topological sense) from those in which they are not, i.e., the first symmetry zeros are not in D_0 . There is then a second separatrix that divides those level sets such that the first and second symmetry zeros are in D_0 . This continues to the third, fourth, etc., symmetry zero. This process of passing through the separatrices as a function of ρ is defined here as *contour budding*. The budding process is a remarkably abrupt function of level set value. (This behavior is difficult to capture in a static image.) Meanwhile, Figure 20 shows the first, second, and third separatrices for the case of $\mathcal{L}(C^{(3)}; z)$. The first separatrix occurs at approximately $|f_{32}(z)| = 0.4645$. One sees that the contours representing level sets less than 0.4645 demarcate D_0 domains that contain the origin as the only zero. For values between approximately 0.4645 and 0.8614, the contours demarcate D_0 domains that now contain the three first symmetry zeros in addition to the domain. Values for the first separatrix level set value and radial position, ρ_S (along $z = \rho e^{i\frac{\pi}{k}}$) for the cases $k = 1, \dots, 12$ are collected in Table 1. The position of the separatrices (especially the first and second) converge very quickly with N . This is not the case for the position of the symmetry zeros which slowly move to the natural boundary with increasing N .

Interestingly, both the ρ_S (left) and separatrix level set values, as a function of k , fit a Langmuir isotherm model $\left(A \frac{x}{x+b} + c\right)$ surprisingly well. These data are plotted in Figure 21 along with the model fit. It is unclear why these data fit the Langmuir isotherm model so well but somehow the model is capturing a “saturation” of ρ_S (left) and $|f_{32}(z_S)|$ as k increases.

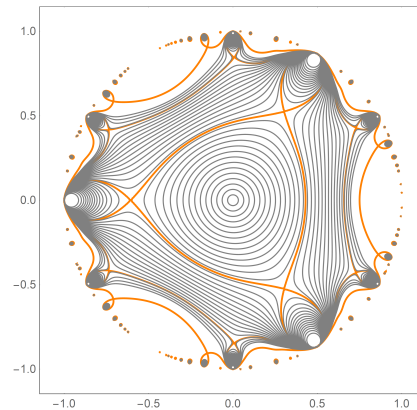


Figure 20. The first, second, and third separatrices for the case of $\mathcal{L}(C^{(3)}; z)$ and $N = 32$ are shown in orange and are superimposed on the contour plot. The value of the level sets occur at approximately $|f_{32}(z)| = 0.4645, 0.8620$, and 1.1275 , respectively.

Table 1. “Exact” values of ρ_{S_i} and corresponding the separatrix level set value, for the first and second separatrix. The “exact” values were calculated using the $N = 32$ member of each lacunary sequence.

k	ρ_{S_1}	$ f_{32}(z_{S_1}) $	ρ_{S_2}	$ f_{32}(z_{S_2}) $
1	0.392403	0.216179	0.688551	0.647672
2	0.531789	0.369646	0.794944	0.795392
3	0.606321	0.464533	0.843906	0.861992
4	0.654943	0.530380	0.872941	0.900589
5	0.690101	0.579452	0.892416	0.925975
6	0.717165	0.617789	0.906488	0.944015
7	0.738884	0.648762	0.917177	0.957529
8	0.756839	0.674420	0.925596	0.968047
9	0.772015	0.696095	0.932413	0.976475
10	0.785063	0.714696	0.938053	0.983384
11	0.796438	0.730866	0.942802	0.989155
12	0.806467	0.745076	0.946858	0.994050

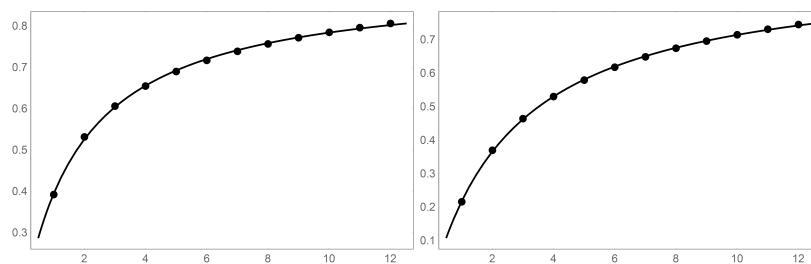


Figure 21. Plots of data for ρ_S (left) and $|f_{32}(z_S)|$ (right) versus k from Table 1. Each data set is fit to a Langmuir isotherm $(A \frac{x}{x+b} + c)$. Fit values: (ρ_S ; $A = 0.7831, b = 1.9360, c = 0.1282$) and ($|f_{32}(z_S)|$; $A = 0.9588, b = 2.7512, c = -0.03738$).

An approximation procedure is now offered for obtaining the separatrix level set value and the corresponding radial position, ρ_S . This procedure will be referred to here as the “quadratic estimate” and “cubic estimate.” One notes that a degenerate point of the separatrix contour lies along the first symmetry angle. Here $z = \rho e^{\frac{i\pi}{k}}$ and the separatrix is a maximum of $|f_N(\rho e^{\frac{i\pi}{k}})|$ along the radial segment running from the origin to the unit circle.

For the quadratic estimate, consider

$$|f_3(\rho e^{\frac{i\pi}{k}})| = \sqrt{\rho^2 - 2\rho^{k+2} + \rho^{2k+2}} + O(\rho^{3k+2}). \tag{48}$$

An estimate can be obtained by truncating the expression as indicated by the “order of” symbol “O.” Now the maximum value of $|f_3(\rho e^{\frac{i\pi}{k}})|$ and, therefore, $|f_N(\rho e^{\frac{i\pi}{k}})|^2$ will occur at the separatrix point. Setting the derivative equal to zero locates that point:

$$0 = \frac{d|f_3(\rho e^{\frac{i\pi}{k}})|^2}{d\rho} = \rho(2 - (2k + 4)\rho^k + (2k + 2)\rho^{2k}). \tag{49}$$

Considering the factor in parenthesis, setting $\rho^k = x$ and solving the resulting quadratic equation yields a remarkably simple expression $x = \frac{1}{k+1}$. Thus,

$$\rho_{\text{est}} = \sqrt[k]{\frac{1}{k+1}}. \tag{50}$$

This produces the estimate of the separatrix level set value

$$|f(z_{\text{est}})| = \sqrt{\left(\sqrt[k]{\frac{1}{k+1}}\right)^2 - 2\left(\sqrt[k]{\frac{1}{k+1}}\right)^{k+2} + \left(\sqrt[k]{\frac{1}{k+1}}\right)^{2k+2}}. \tag{51}$$

The quadratic estimate values for ρ_{est} and $|f(z_{\text{est}})|$ are collected in Table 2 along with a %error which is calculated by comparison to the “exact” values listed in Table 1.

Table 2. Quadratic (left set) and cubic (right set) estimated values of ρ_s and corresponding separatrix level set value, for the first separatrix. The percent error is given relative to the “exact” values from Table 1.

k	ρ_{est}	%error	$ f(z_{\text{est}}) $	%error	ρ_{est}	%error	$ f(z_{\text{est}}) $	%error
1	0.500000	27.4	0.250000	15.6	0.344334	−12.3	0.203199	−6.00
2	0.577350	8.57	0.384900	4.13	0.515208	−3.12	0.365099	−1.23
3	0.629961	3.90	0.472470	1.71	0.599184	−1.18	0.462625	−0.41
4	0.668740	2.11	0.534992	0.87	0.651413	−0.54	0.529459	−0.17
5	0.698827	1.26	0.582356	0.50	0.688176	−0.28	0.578958	−0.09
6	0.723020	0.82	0.619731	0.31	0.716035	−0.16	0.617503	−0.05
7	0.742997	0.56	0.650123	0.21	0.738181	−0.10	0.648585	−0.03
8	0.759836	0.40	0.675409	0.15	0.756380	−0.06	0.674305	−0.02
9	0.774264	0.29	0.696837	0.11	0.771703	−0.04	0.696018	−0.01
10	0.786793	0.22	0.715267	0.08	0.784845	−0.03	0.714642	−0.01
11	0.797797	0.17	0.731314	0.06	0.796281	−0.02	0.730827	−0.01
12	0.807554	0.13	0.745434	0.05	0.806351	−0.01	0.745047	0.00

One can obtain a better estimate by adding a term in the truncated expression, Equation (48). This is referred to here as the cubic estimate. Progressing in the same way as for the quadratic estimate leads to a much more elaborate expression for ρ_{est} (not shown here). With the aid of MATHEMATICA, one calculates the values given in Table 2. One notes that both types of estimates improve as k increases. It is also the case that the quadratic estimate is too high and the cubic estimate is too low.

The case of $k = 3$ serves as an illustrative example for the quadratic estimate procedure. One employs the N th member of the lacunary sequence:

$$\begin{aligned} |f_3(\rho e^{\frac{i\pi}{3}})| &= \sqrt{\left(\rho e^{\frac{i\pi}{3}} + \rho^4 e^{\frac{4i\pi}{3}} + \rho^{10} e^{\frac{10i\pi}{3}}\right) \left(\rho e^{-\frac{i\pi}{3}} + \rho^4 e^{-\frac{4i\pi}{3}} + \rho^{10} e^{-\frac{10i\pi}{3}}\right)} \\ &= \sqrt{(\rho^2 - 2\rho^5 + \rho^8 + O\rho^{11})}, \end{aligned} \tag{52}$$

where properties of exponents and their representations of -1 have been used. The derivative of $(\rho^2 - 2\rho^5 + \rho^8)$ yields an equation for estimating the position of the maximum

$$\begin{aligned}
 2\rho - 10\rho^4 + 8\rho^7 &= 0 \\
 \rho(2 - 10\rho^3 + 8\rho^6) &= 0.
 \end{aligned}
 \tag{53}$$

Solving this gives the non-zero $\rho_{\text{est}} = \sqrt[3]{\frac{1}{4}} = 0.6300$. Comparing this to the “exact” value in Table 1, one calculates a percent error of 3.9%. Substituting $\rho_{\text{est}} = 0.6300$ into $|f(z_{\text{est}})| = \sqrt{(\rho^2 - 2\rho^5 + \rho^8)}$ yields the first separatrix value of 0.4725 (%error = 1.7%). When the estimate is done at the cubic level, one obtains $\rho_{\text{est}} = 0.5992$ (−1.18 %error) and $|f(z_{\text{est}})| = 0.4626$ (−0.41 %error).

10.2. Scaling

One can put Theorem 2 to use as an approximation method based on expressing approximate versions of $\mathcal{L}(C^{(k)}; z)$ in terms of $\mathcal{L}(C^{(2)}; z)$. The reason one might want to do this is that the N th $C^{(k)}$ is much greater than that for $C^{(2)}$ as N gets large or as k gets large. Consequently, one must numerically compute numbers raised to much higher powers than is needed for the $k = 2$ case. This may be useful in some applications so a procedure for this is now described.

One can recast the main unity contour as a plot of $\rho(\phi)$ versus ϕ . This is shown in Figure 22 for the cases of $\mathcal{L}(C^{(2)}; z)$ and $\mathcal{L}(C^{(4)}; z)$. Doing this clearly exposes the rotational symmetry (and mirror symmetry for that matter) of $\mathcal{L}(C^{(k)}; z)$. Also clearly exposed is the relation between $\mathcal{L}(C^{(2)}; z)$ and $\mathcal{L}(C^{(k)}; z)$ (in this case $k = 4$) as given by Theorem 2. The $k > 2$ case has the same basic functional shape as $k = 2$ when $\phi \rightarrow \frac{k}{2}\phi$. However, it is not a simple multiplication of angle transformation. The dotted curve in the bottom right panel of Figure 22 shows $\mathcal{L}(C^{(2)}; \rho e^{i2\phi})$ superimposed on the $\mathcal{L}(C^{(4)}; \rho e^{i\phi})$ case. The dotted curve must be scaled to approximate the $\mathcal{L}(C^{(4)}; \rho e^{i\phi})$ case.

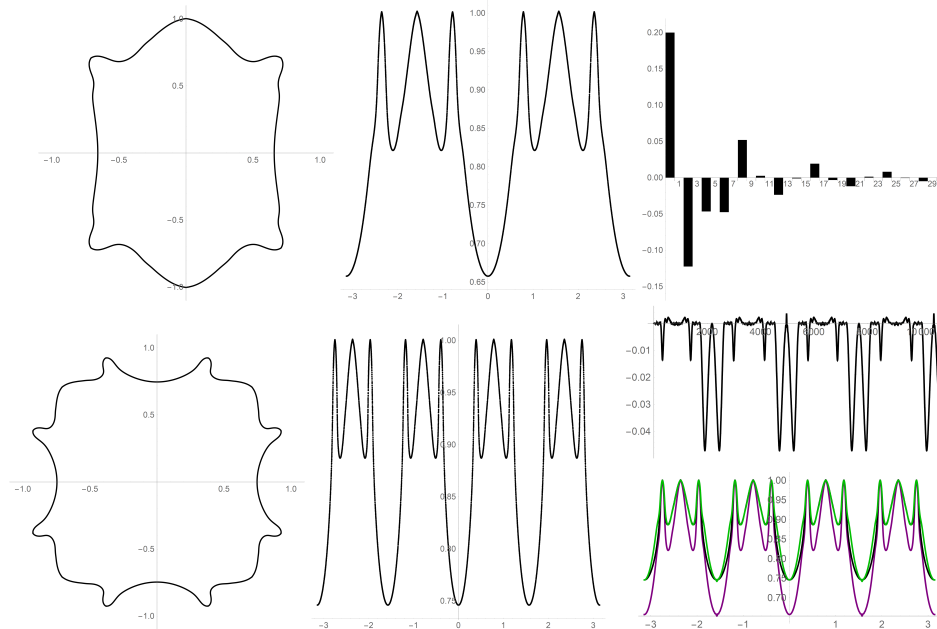


Figure 22. Analysis related to scaling of $\mathcal{L}(C^{(2)}; z)$ to $\mathcal{L}(C^{(k)}; z)$ (in this case $k = 4$). The top row of panels pertain to the main unity contour for $\mathcal{L}(C^{(2)}; z)$. The top left shows the main unity contour. This translated to a $\rho(\phi)$ versus ϕ plot in the middle panel. The top right panel shows the Fourier decomposition of the curve in the middle panel (the constant coefficient is 0.84 but has been cut off at 0.2 in order to show the other coefficients more clearly). The bottom left and middle panels are the analog of the top left and middle panels but for $\mathcal{L}(C^{(4)}; z)$. The bottom right panel shows $\mathcal{L}(C^{(4)}; \rho e^{i\phi})$ (black), $\mathcal{L}(C^{(2)}; \rho e^{i2\phi})$ (purple), and quadratically scaled $\mathcal{L}(C^{(2)}; \rho e^{i2\phi})$ (green), ($a_1 = 0.50607$ and $a_2 = -0.33248$). Finally, the residual is shown as well.

To obtain complete agreement between the curves requires an infinite series because of the relationship of Theorem 2. However, one is able to get relatively good approximate agreement by forcing agreement at three points: unity, and the two different trough values. Fairly good agreement is achieved at the “quadratic” level scaling factor of the form $a_1(1 - \rho) + a_2(1 - \rho)^2$. The superimposed dashed curve is the quadratically scaled ($a_1 = 0.50607$ and $a_2 = -0.33248$) $\mathcal{L}(C^{(2)}; \rho e^{i2\phi})$ curve. The residual (solid minus dashed) is plotted above the graph. The residual indicates that the regions of greatest error occur from the scaled $k = 2$ curve being slightly narrower than the $k = 4$ curve coming out of the troughs.

The base radial structure (top middle panel of Figure 22) is a particularly illuminating way to touch base with the discussion from Section 4 regarding the limiting case of $k \rightarrow \infty$. That base structure gets scaled and repeated as k increases and thus one readily sees the regularity of the natural boundary in the $k \rightarrow \infty$ limit. One also sees the manner in which the symmetry zeros and intervening infinities converge onto themselves.

As a secondary note on the nature of $\mathcal{L}(C^{(2)}; z)$ not related to the above discussion, one can Fourier analyze the $\rho(\phi)$ curve. This reveals the absence of all of the odd terms. This consistent with the 2-fold rotational symmetry of $\mathcal{L}(C^{(2)}; \rho e^{i2\phi})$. The Fourier spectrum is shown in the top right panel of Figure 22.

10.3. Integration

Although a bit off the central focus of this paper, one would be remiss if one did not investigate complex contour integration of lacunary functions inside the open unit disk. The lacunary functions built on cpns suggest certain special integration paths to explore. Only the paths along the symmetry angles and paths running along the natural boundary between adjacent symmetry angles are considered here.

Because the limit point set is bounded as $N \rightarrow \infty$ and converges to zero all $\rho < 1$, one can get a meaningful integration value. Plots of the $\mathcal{L}(C^{(3)}; e^{\frac{i\pi}{3p}})$ for the first six symmetry angles are shown in Figure 23. The values of the integral along the first 20 symmetry paths are plotted in the bottom right panel of Figure 23. There is an early increase in both the real and imaginary integral values with p . The integral value of real part continues to increase with increasing p whereas the imaginary part peaks at $p = 3$. In each case the rate of change of the integration value with p slows considerably.

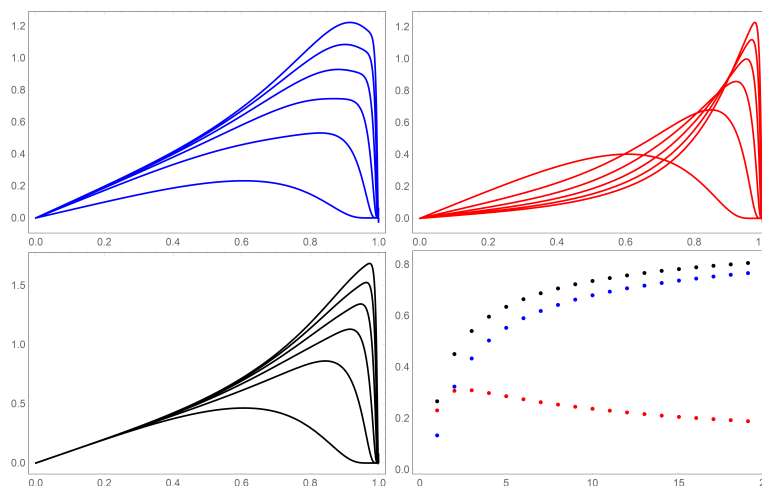


Figure 23. Plots of the real (blue), imaginary (red) and modulus (black) of $f_{50}(z)$ for the first six symmetry angles and for $k = 3$. In all cases, the graphs skew toward unity and increase in maximum value as the symmetry angle increases (The top curve in each case corresponds to $p = 6$ whereas the bottom curve corresponds to $p = 1$). The bottom right panel shows the value of the integral of the real (blue), imaginary (red) and modulus (black) of $f_{50}(z)$ as a function of symmetry angle, p .

One can consider the integration path

$$\oint f_N(z) = \int_{p=i} f_N(z) + \int_{\frown} f_N(z) - \int_{p=j} f_N(z), \tag{54}$$

where $\int_{p=i}$ means integration from the origin to the natural boundary along the $p = i$ symmetry angle, \int_{\frown} means integration along an arc of the natural boundary from symmetry angle i to j , and $i < j$ (to produce a counterclockwise integration path). Since $f_N(z)$ is analytic for all N on the interior of the unit disk, $\oint f_N(z) = 0$ by Cauchy's theorem and thus,

$$\int_{\frown} f_N(z) = \int_{p=j} f_N(z) - \int_{p=i} f_N(z). \tag{55}$$

11. Conclusions

Lacunary sequences were investigated, with special attention paid to the $\mathfrak{L}(C^{(k)}; z)$ family. The special characteristics of the cpns lead to true rotational symmetry of $|f_N(z)|$ and to the polished nature of its main unity contour. This was compared with other lacunary sequences which exhibit only quasi-rotational symmetry and are not polished. The level sets of $|f_N(z)|$ were particularly illuminating for this work. Two particular mappings of the lacunary functions onto a sphere were discussed. The inverse stereographic projection maps the natural boundary to the equator. The second mapping discussed allows for the natural boundary to be condensed into a point at the south pole.

The behavior and characteristics of the natural boundary for centered polygonal lacunary sequences were discussed. While these systems are extremely complicated, they are well organized because of the inherent rotational symmetry of the centered polygonal lacunary functions. This is particularly apparent at the symmetry angles. Here, the value at the natural boundary follows a relatively simple $4p$ -cycle. Fibered spaces can organize these cycles into equivalence classes. This then provides a natural way to approach $N = \infty$.

Specific attention was given to the p -sequences of centered polygonal lacunary functions. These special sequences have many interesting characteristics. Understanding these characteristics aids in providing overall insight into the centered polygonal lacunary functions themselves. A fiber bundle based description of the p -sequences; the cross-sections on the fiber bundle itself and the associated fiber position diagram. Symmetry and autocorrelation analysis of the fiber position diagrams brought some the features of the centered polygonal functions to the fore.

Several relationships amongst lacunary functions were presented. The phenomenon of contour budding was studied, as was an investigation of the positions of separatrices in the contour plots of $|f_N(z)|$. A procedure for making estimates about these separatrices was given. Several lemmas and theorems on the nature of the limit points at the natural boundary at the symmetry angles were also given and discussed.

It is hoped that the insight in lacunary sequences provided by this work can serve as a foundation for future work with centered polygonal lacunary sequences, particularly for researchers interested in their use in analysis of physical problems. Perhaps a particularly interesting direction to explore would be the application of sequences related to the partition function. Indeed, the lacunary sequence built from the triangular numbers themselves is very closely related to the partition function for the quantum rigid rotor model from physics and chemistry. Perhaps the centered polygonal lacunary sequences can form an interesting generalization of these partition functions. Certainly, some mathematical directions to go in would be to consider the Laurent version of these series or to generalize to

$$f_N(z) = \sum_{n=1}^N a_{g(n)} z^{g(n)}. \tag{56}$$

Finally, it would be interesting to investigate the nature of the cpns and what their properties make manifest in the lacunary functions. For example, it is noted but not explored here that sets created by unions of cpn sets are also smooth but intersections are not. Further, certain unions even maintain true rotational symmetry.

Author Contributions: K.S. and D.J.U. conceived the investigation; K.S. and D.J.U. designed the investigation. K.S. and D.J.U. provided background for the investigation; D.J.U. wrote the MATHEMATICA code to perform the investigation; D.R. developed distributed computing capabilities; K.S., D.R. and D.J.U. analyzed the data; K.S. and D.J.U. wrote the original draft of manuscript; K.S., D.R. and D.J.U. edited the manuscript.

Funding: This research was funded by the Concordia College Chemistry Endowment Fund.

Acknowledgments: We thank Douglas R. Anderson and Laura LeGare for valuable discussion.

Conflicts of Interest: The authors declare no conflict of interest. The funders had no role in the design of the study; in the collection, analyses, or interpretation of data; in the writing of the manuscript, or in the decision to publish the results.

References

- Hille, E. *Analytic Function Theory Vol. II*; Ginn and Company: Boston, MA, USA, 1962.
- Kahane, J.-P. A century of interplay between Taylor series, Fourier series and Brownian motion. *Bull. Lond. Math. Soc.* **1997**, *29*, 257–279. [[CrossRef](#)]
- Hille, E. *Analytic Function Theory, Vol. I*; Ginn and Company: Boston, MA, USA, 1959.
- Creagh, S.C.; White, M.M. Evanescent escape from the dielectric ellipse. *J. Phys. A* **2010**, *43*, 465102. [[CrossRef](#)]
- Greene, J.M.; Percival, I.C. Hamiltonian maps in the complex plane. *Physica D* **1981**, *3*, 530–548. [[CrossRef](#)]
- Shudo, A.; Ikeda, K.S. Tunneling effect and the natural boundary of invariant tori. *Phys. Rev. Lett.* **2012**, *109*, 154102. [[CrossRef](#)]
- Guttman, A.J.; Enting, I.G. Solvability of some statistical mechanical systems. *Phys. Rev. Lett.* **1996**, *76*, 344–347. [[CrossRef](#)]
- Orrick, W.P.; Nickel, B.G.; Guttman, A.J.; Perk, J.H.H. Critical behavior of the two-dimensional Ising susceptibility. *Phys. Rev. Lett.* **2001**, *86*, 4120–4123. [[CrossRef](#)]
- Nickel, B. On the singularity structure of the 2D Ising model susceptibility. *J. Phys. A Math. Gen.* **1999**, *32*, 3889–3906. [[CrossRef](#)]
- Yamada, H.S.; Ikeda, K.S. Analyticity of quantum states in one-dimensional tight-binding model. *Eur. Phys. J. B* **2014**, *87*, 208. [[CrossRef](#)]
- Jensen, G.; Pommerenke, C.; Ramirez, J.M. On the path properties of a lacunary power series. *Proc. Am. Math. Soc.* **2014**, *142*, 1591–1606. [[CrossRef](#)]
- Aistleitner, C.; Berkes, I. On the central limit theorems for $f(n_k x)$. *Probab. Theory Relat. Fields* **2010**, *146*, 267–289. [[CrossRef](#)]
- Fukuyama, K.; Takahashi, S. The central limit theorem for lacunary series. *Proc. Am. Math. Soc.* **1999**, *127*, 599–608. [[CrossRef](#)]
- Salem, P.; Zygmund, A. On lacunary trigonometric series. *Proc. Natl. Acad. Sci. USA* **1947**, *33*, 333–338. [[CrossRef](#)] [[PubMed](#)]
- Blendeck, T.; Michaliček, J. L^1 -norm estimates of character sums defined in a Sidom set in the dual of a Kac algebra. *J. Oper. Theory* **2013**, *70*, 375–399. [[CrossRef](#)]
- Wang, S. Lacunary Fourier series for compact quantum groups. *Commun. Math. Phys.* **2017**, *349*, 895–945. [[CrossRef](#)]
- Lehmer, D.H. Incomplete Gaussian sums. *Mathematika* **1976**, *23*, 125–135. [[CrossRef](#)]
- Paris, R.B. An asymptotic approximation for incomplete Gauss sums. *J. Comput. Appl. Math.* **2008**, *212*, 16–30. [[CrossRef](#)]
- Kerr, B. Incomplete gauss sums modulo primes Q . *J. Math.* **2018**, *69*, 729–745. [[CrossRef](#)]
- Shparlinski, I.E. On sums of Kloosterman and Gauss sums. *Trans. Am. Math. Soc.* **2019**, *371*, 8679–8697. [[CrossRef](#)]
- Coutsias, E.A.; Kazarinoff, N.D. Disorder, renormalizability, theta functions and Cornu spirals. *Physica D* **1987**, *26*, 295–210. [[CrossRef](#)]
- Rainville, E.D. *Special Functions*; Chelsea Pub. Co.: New York, NY, USA, 1971.

23. Bellman, R. *A Brief Introduction to Theta Functions*; Dover Pub.: Mineola, NY, USA, 2013.
24. Abramowitz, M.; Stegun, I.A. *Handbook of Mathematical Functions*; Dover Publications: New York, NY, USA, 1972.
25. Schlicker, S.J. Numbers simultaneously polygonal and centered polygonal. *Math. Mag.* **2011**, *84*, 339–350. [[CrossRef](#)]
26. Mork, L.K.; Vogt, T.; Sullivan, K.; Rutherford, D; Ulness, D.J. Exploration of filled-In Julia sets arising from centered polygonal lacunary functions. *Fractal Fract.* **2019**, *3*, 42. [[CrossRef](#)]
27. Vogt, T; Ulness, D.J. Cornu spirals and the triangular lacunary trigonometric system. *Fractal Fract.* **2019**, *3*, 40. [[CrossRef](#)]
28. Yamada, H.S.; Ikeda K.S. A numerical test of Padé approximation for some functions with singularity. *Int. J. Comput. Math.* **2014**, *2014*, 587430. [[CrossRef](#)]
29. Teo, B.K.; Sloane, J.A. Magic numbers in polygonal clusters. *Inorg. Chem.* **1985**, *24*, 4545–4558. [[CrossRef](#)]
30. Kahane, J.-P. Lacunary Taylor and Fourier series. *Bull. Am. Math. Soc.* **1964** *70*, 199–213. [[CrossRef](#)]
31. Vartziotis, D.; Bohnet, D. Fractal curves from prime trigonometric series. *Fractal Fract.* **2018**, *2*, 2. [[CrossRef](#)]
32. Diamond, F.; Shurman, J. *A First Course in Modular Forms*; Springer: New York, NY, USA, 2005.
33. Structure and Properties of the Triangular Numbers Modulo m . Available online: www.researchgate.net/publication/334389220_Structure_and_properties_of_the_triangular_numbers_modulo_m (accessed on 10 October 2019).
34. Steenrod, N. *The Topology of Fibre Bundles*; Princeton Univ. Press: Princeton, NJ, USA, 1950.



© 2019 by the authors. Licensee MDPI, Basel, Switzerland. This article is an open access article distributed under the terms and conditions of the Creative Commons Attribution (CC BY) license (<http://creativecommons.org/licenses/by/4.0/>).